

Theory of correlated insulators and superconductivity in twisted bilayer graphene

Gal Shavit, Erez Berg, Ady Stern, and Yuval Oreg

Department of Condensed Matter Physics, Weizmann Institute of Science, Rehovot, Israel 76100

(Dated: April 1, 2025)

We introduce and analyze a model that sheds light on the interplay between correlated insulating states, superconductivity, and flavor-symmetry breaking in magic angle twisted bilayer graphene. Using a variational mean-field theory, we determine the normal-state phase diagram of our model as a function of the band filling. The model features robust insulators at even integer fillings, occasional weaker insulators at odd integer fillings, and a pattern of flavor-symmetry breaking at non-integer fillings. Adding a phonon-mediated inter-valley retarded attractive interaction, we obtain strong-coupling superconducting domes, whose structure is in qualitative agreement with experiments. Our model elucidates how the intricate form of the interactions and the particle-hole asymmetry of the electronic structure determine the phase diagram. It also explains how subtle differences between devices may lead to the different behaviors observed experimentally. A similar model can be applied with minor modifications to other moiré systems, such as twisted trilayer graphene.

Introduction.— When two graphene layers are stacked at a relative twist angle of $\sim 1.1^\circ$, the lowest lying electron bands become exceptionally flat [1]. In recent years, this so-called magic angle twisted bilayer graphene (MATBG) emerged as a highly tunable platform to study strongly correlated physics. Correlated insulators (CIs), where electronic interactions induce a gap and suppress transport, have been first experimentally observed in MATBG at fillings of $\nu = \pm 2$ electrons relative to the charge neutrality point (CNP) per moiré unit cell [2, 3]. Later experiments found a CI also at $\nu = +3$ [4, 5], and in some instances CIs were measured at nearly all integer fillings [6]. In most experiments the insulating behavior is more pronounced for electrons ($\nu > 0$). The possible origin of these integer-filling CIs has been explored in several recent works [7–14].

Another remarkable feature of MATBG is the appearance of superconducting domes near the CIs at $\nu = \pm 2$ [3–5], with superconductivity generally being more robust for holes ($\nu < 0$), and (for both electrons and holes) on the $|\nu| > 2$ side. A series of recent experiments which manipulated the electrostatic screening have indicated that Coulomb repulsion is either detrimental to superconductivity in MATBG or weakly affects it [4, 5, 15, 16]. This suggests that electron-phonon coupling may play a role in MATBG [17–21], and plausibly induce superconductivity at certain fillings. Yet, as we show here, the interplay between strong repulsion, retarded attraction due to phonons, and the unique multi-band structure may lead to non-conventional superconducting order parameter.

In this manuscript, we introduce and investigate a phenomenological model and find that it exhibits the most salient features of MATBG observed in experiments. The model is comprised of four electronic “flavors”, accounting for spin and valley (K and K') degeneracies, and interactions with strengths of the order of their bandwidth. The structure of the interaction terms and the features of the density of states (DOS) of non-interacting MATBG determine the phase diagram.

We find that electron correlations generically induce CIs at even integer fillings with inter-valley coherent (IVC) order (i.e., spontaneously breaking valley $U_v(1)$ symmetry), whereas the odd-integer CIs, typically having bands with non-zero Chern numbers, are more sensitive to details of sub-

leading interaction terms. At non-integer fillings, the system is not fully gapped, yet, the spin-valley flavor symmetry is broken [22–24]. Retarded inter-valley attractive interactions, due to e.g., phonons [18], then enable the formation of superconducting domes, which are most prominent in our model at fillings which agree remarkably well with experiments. As depicted in Fig. 1, we recover a superconducting dome flanked by two insulating states near $\nu = +2, +3$, and a more substantial dome on the hole-doped side of the $\nu = -2$ CI.

Using renormalization group (RG) tools we explore the interplay of Coulomb interactions and the retarded attraction (employing the so-called Tolmachev-Anderson-Morel RG [25, 26]), accounting for the structured electronic DOS of the MATBG and phonons at all scales on the superconducting transition temperature T_c . At certain fillings, strong-coupling superconductivity may be established, i.e., T_c becomes an appreciable fraction of the Fermi temperature T_F , leading to significant superconducting phase fluctuations, whose effect on transport we account for. This is enabled by the underlying normal state, where interactions induce spontaneous breaking of flavor-symmetry and the valley $U_v(1)$ symmetries. Moreover, this symmetry-broken state has only two active flavors in different valleys and opposite spins, hence we expect that it will sustain large in-plane magnetic fields, whose magnitude is determined by the details of the normal-state interaction.

Physical effects neglected in the model that may be important in certain regimes and possible extensions are discussed in the concluding remarks.

Model and results.— We begin with a model comprised of eight flat bands with valley (K/K'), spin, and sublattice (A/B) degrees of freedom, labeled by Pauli matrices τ_i , s_i , and σ_i , respectively. This choice of basis is motivated by the MATBG sublattice-polarized basis discussed in Ref. [10]. These bands have a valley-dependent Chern number, $C = \tau_z \sigma_z$, which can be understood from the two chiral Dirac cones in each valley. The model Hamiltonian is

$$H = \sum_{\mathbf{k}} \Psi_{\mathbf{k}}^\dagger h_0(\mathbf{k}) \Psi_{\mathbf{k}} + H_{\text{int}}, \quad (1)$$

where H_{int} describes the interactions (to be discussed shortly), $\Psi_{\mathbf{k}}$ is an 8-spinor of fermionic operators $c_{\tau s \sigma}(\mathbf{k})$ (annihilating an electron at valley τ , spin s and sub-lattice σ),

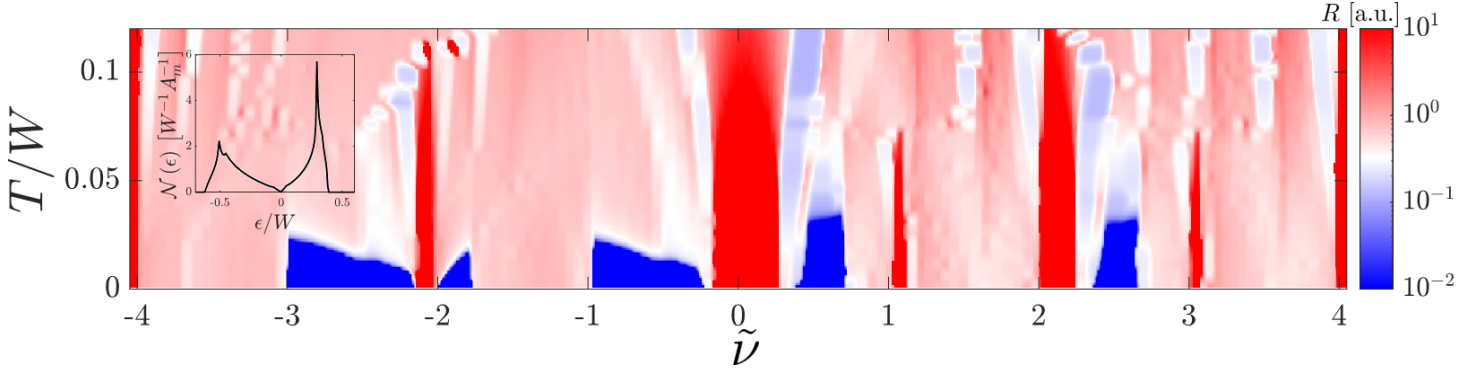


FIG. 1. Temperature and filling ($\tilde{\nu}$, see SM Sec. S.3) dependent phase diagram of the model. We plot the resistivity, which is inversely proportional to the compressibility far from the superconducting phase, see SM Sec. S.5. The model features CIs near certain integer fillings and superconducting domes, both in qualitative agreement with experiments. We have used the interaction parameters [see Eq. (3)] $U_C = 0.7W$, $U_\delta = 0.15W$, $g_1 = g_2 = 0.12W$, and phonon-mediated attraction strength [see Eq. (6)] $V^* = 0.24W$. Inset: the DOS produced by the single-particle Hamiltonian (2). For a detailed schematic phase diagram, see SM.

and the single-particle term is

$$h_0(\mathbf{k}) = f_x(\mathbf{k})\sigma_x + f_y(\mathbf{k})\sigma_y\tau_z + f_{p-h}(\mathbf{k}). \quad (2)$$

The functions f_x , f_y , and f_{p-h} determine the dispersion in the moiré Brillouin zone (mBZ), which has two Dirac cones with the same chirality, and reproduces an electronic DOS with the prominent features associated with the flat bands of MATBG (see inset to Fig. 1). Namely, a linear increase in the DOS near the CNP, a pronounced DOS peak near half-filling of the conduction/valence bands followed by a decline towards the band edge, and appreciable particle-hole asymmetry (captured by f_{p-h}). The combined bandwidth of the conduction and valence bands in the mBZ is W . We note that the form of $h_0(\mathbf{k})$ preserves $C_2 = \tau_x\sigma_x$ and time-reversal symmetry $\mathcal{T} = \tau_x\mathcal{K}$, with \mathcal{K} the complex-conjugation operator [27]. For more details about $h_0(\mathbf{k})$, see Supplementary Materials (SM), Sec. S.1 A [28].

We write electron-electron interactions as a sum of local interaction terms,

$$H_{\text{int}} = \sum_{\alpha, \mathbf{k}, \mathbf{k}', \mathbf{q}} \frac{\lambda_\alpha}{2\Omega} \left(\Psi_{\mathbf{k}+\mathbf{q}}^\dagger \vec{\mathcal{O}}_\alpha \Psi_{\mathbf{k}} \right) \cdot \left(\Psi_{\mathbf{k}'-\mathbf{q}}^\dagger \vec{\mathcal{O}}_\alpha \Psi_{\mathbf{k}'} \right), \quad (3)$$

where Ω is the volume, $\vec{\mathcal{O}}_\alpha$ are matrices in valley-spin-sublattice space, and λ_α are the appropriate coupling constants. The most dominant term is the density-density interaction with $\vec{\mathcal{O}}_1 = \mathbf{1}$, $\lambda_1 = U_C$, whose magnitude reflects the screened Coulomb repulsion. We consider a secondary interaction $\vec{\mathcal{O}}_2 = (\tau_z\sigma_x, \sigma_y)$ with $\lambda_2 = U_\delta$, accounting for the form-factors obtained when projecting the Coulomb interaction onto the MATBG flat bands away from the chiral limit [10]. Additional secondary terms are inspired by instantaneous interactions due to electron-optical-phonon interactions, captured by $\vec{\mathcal{O}}_3 = (\sigma_y\tau_z, \sigma_x)$ with $\lambda_3 = g_1$, and $\vec{\mathcal{O}}_4 = (\tau_x\sigma_x, \tau_y\sigma_x)$ with $\lambda_4 = g_2$. Their structure is dictated by the electron-phonon coupling to low-momentum phonons ($\vec{\mathcal{O}}_3$) and to phonons carrying valley-momentum ($\vec{\mathcal{O}}_4$) [17]. The phonon-induced interactions are attractive,

i.e., $g_1, g_2 < 0$. We note that the interactions preserve C_2 , \mathcal{T} , and $C_3 = e^{2\pi i/3}\sigma_z\tau_z$ symmetries [29].

We study the model (1)–(3) using a variational Hartree-Fock approach. We minimize the grand-potential Φ , at a given temperature T and chemical potential μ , generated by the variational Hamiltonian $H_{\text{MF}} = \sum_{\mathbf{k}} \Psi_{\mathbf{k}}^\dagger h_{\text{MF}}(\mathbf{k}) \Psi_{\mathbf{k}}$, see SM, Eq. (S10) [28]. We note that in the mean-field approach, due to the local nature of the interactions, the details of the non-interacting dispersion do not play a role, only the DOS.

We explore three kinds of spontaneous symmetry breaking in h_{MF} : (i) Flavor-symmetry breaking, i.e., one or several of the operators $\{s_z, \tau_z, \tau_z s_z\}$ attain a finite expectation value; (ii) intra-flavor sublattice-symmetry breaking (σ_z terms), leading to Chern gaps; (iii) IVC order with a finite expectation value for $\tau_x \cos \gamma + \tau_y \sin \gamma$ (the angle γ breaks the valley $U_v(1)$ symmetry). We restrict our analysis to IVC terms of the form

$$\Delta_{\text{ivc}}^\pm \frac{1 \pm s_z \tau_z}{2} \tau_y s_x \sigma_y, \quad (4)$$

(implicitly choosing $\gamma = \pi/2$). This order-parameter resembles the Kramers-IVC of Ref. [10], with an effective time-reversal symmetry $\mathcal{T}' = \tau_y s_x \mathcal{K}$. The sublattice-off-diagonal form of this term ensures coupling of bands with the same Chern number $C = \tau_z \sigma_z$, which is energetically favorable [30]. The choice of $s_x \sigma_y$ in (4) is justified *a posteriori* by examination of the interaction energy within the mean-field state; for details of the analysis, see SM Sec. S.1 B [28]. We find that the g_2 interaction favors orders where the spin is anti-aligned in opposite valleys, justifying s_x in Eq. (4). Moreover, we find that U_δ and g_1 favor states where $\langle c_{\tau s \sigma}^\dagger c_{\bar{\tau} \bar{s} \bar{\sigma}} \rangle = -\langle c_{\tau s \bar{\sigma}}^\dagger c_{\bar{\tau} \bar{s} \sigma} \rangle^*$, so IVC orders $\propto \sigma_y$ gain interaction energy. Lastly, our analysis suggests sublattice-symmetry breaking is favored by g_1 , yet *suppressed* by U_δ . The interplay between these two interactions is key to understanding why insulators at odd filling factors are experimentally less robust as compared to those at even filling.

Results for the mean-field phase diagram are shown in Fig. 2. In panels (a)–(b) we plot the filling per moiré unit

cell ν_i of each flavor, for different values of U_δ and g_1 . Our results feature a sequence of symmetry-breaking phase transitions. At the CNP, the system is gapped and is in an IVC state where both $\Delta_{\text{IVC}}^\pm \approx 0.34W$. With increased μ , the IVC gap in one $\tau_z s_z$ sector closes, and the two flavors making up that sector begin to fill up [near $(\mu - \mu_{\text{CNP}})/W \approx 0.4$ in Fig. 2 panels (a) and (b)]. This is followed by flavor-symmetry breaking within that sector (blue and red curves split), where one flavor is depleted and the other is filled. Depending on details, the depleted flavor may develop a Chern gap (plateau of red curve at zero), leading to an incompressible region near $\nu = 1$. Increasing μ further, this flavor is gradually filled. This schematic process repeats for the flavors in the other IVC sector (yellow and purple curves starting at $\nu = 2$), following an incompressible regime, where two flavors are completely filled, and two others are IVC-gapped.

We note that in a region around $\nu = 1$, flavor-polarization develops in the gapped IVC sector (yellow and purple), yet it remains incompressible. This is caused by the spin-polarization in the more populated sector (blue and red), promoting opposite polarization in the opposing valley, gaining interaction energy $\propto |g_2|$, as discussed following Eq. (4).

In Fig. 2(c) we plot the compressibility $d\nu/d\mu$ as a function of $\alpha \equiv \frac{U_\delta - g_1}{U_\delta + g_1}$ and $\tilde{\nu}$. The latter is a proxy for the filling fraction which better represents the experimental scenario, where typically a back-gate voltage tunes the electron filling, see SM Sec. S.3 [28]. As α increases, i.e., g_1 becomes smaller as compared to U_δ , the gaps near odd filling close and eventually vanish at $\alpha \sim 0.7$, giving way to finite but low compressibility reminiscent of Ref. [23]. This trend is in line with our analytical examination of the role of U_δ and g_1 . The incompressible IVC states at $\tilde{\nu} = 0, 2$ weakly depend on α , and are thus expected to be more stable.

The phase diagram we obtain establishes that the appearance of insulating states either at all integer fillings, or only at even integer fillings, depends delicately on the details and hierarchy of the effective interaction terms. This sensitivity is a common feature in systems displaying quantum Hall ferromagnetism [31, 32], a phenomenon which is arguably pertinent to the theory of MATBG. We note that the appearance of σ_y -IVC orders at even fillings agrees with the predictions of Ref. [10] and was verified numerically [33]. This is expected as the U_δ interaction captures the effect of the density form-factors of the projected flat bands. Our model thus provides a tractable way to go beyond specific integer fillings and track the evolution of the mean-field ground-state with μ .

Superconductivity.— Our starting point of examining superconductivity in MATBG is the symmetry-breaking cascade obtained from the variational Hartree-Fock approach. We explore inter-valley pairing mediated by electron-phonon interactions. The inter-valley pairing is favored both by the acoustic phonons [18] and since intra-valley Cooper pairs have finite-momentum. Due to this inter-valley attraction, we focus on valley-degenerate areas in the phase diagram. We note that we do not consider scenarios where the superconducting condensation energy gain is sufficient to depolarize opposite-valley flavors.

As discussed, the model favors inter-valley antiferromag-

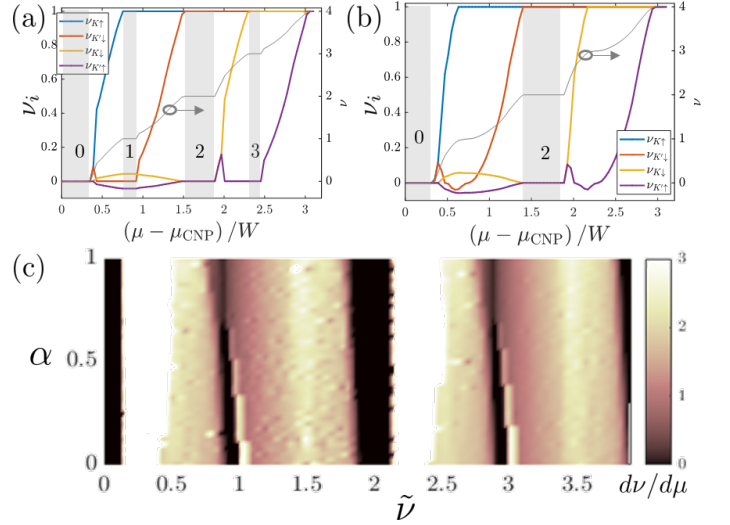


FIG. 2. (a) Zero temperature mean-field occupation per unit cell ν_i of individual flavors and total filling ν as a function of the chemical potential (relative to the CNP). Grey areas mark incompressible regions. The interaction parameters used: $U_C = 0.75W$, $U_\delta = g_1 = 0.1W$, $g_2 = 0.08W$. (b) Same as panel (a), with $U_\delta = 0.2W$ and $g_1 = 0$. The incompressible states at odd integer fillings give way to a “reset” of the Fermi level to the Dirac points. (c) Compressibility $d\nu/d\mu$ as a function of $\tilde{\nu}$ (see SM, Sec. S.3) and $\alpha \equiv \frac{U_\delta - g_1}{U_\delta + g_1}$, retaining $U_\delta + g_1 = 0.2W$, and all other parameters from panels (a)–(b). Notice (a) corresponds to $\alpha = 0$ and (b) to $\alpha = 1$.

netism, and thus prefers opposite-spin pairing. Restricting our discussion to the simplest scenario where the pairing lacks sublattice-structure (since it is sufficient to capture the most salient experimental features), we study the pairing amplitude $\Delta_{\tau\sigma} = \Delta_{\tau SA} = \Delta_{\tau SB}$, where

$$\Delta_{\tau\sigma} = \frac{1}{\Omega} \sum_{\mathbf{k}} \langle c_{\bar{\tau}\bar{\sigma}}(-\mathbf{k}) c_{\tau\sigma}(\mathbf{k}) \rangle. \quad (5)$$

We note that due to the aforementioned spontaneous spin-valley locking and flavor-symmetry breaking, the system attains non-zero spin-triplet pairing correlations [34]. This may lead to phenomenology similar to that of Ising superconductors, namely a critical in-plane magnetic field that is set by the energetics of the normal-state, exceeding the Pauli-Chandrasekhar-Clogston limit [35–37].

We adopt a Tolmachev-Morel-Anderson RG approach [25, 26], allowing us to account for the effects of Coulomb repulsion as well as the phonon-mediated attraction. Neglecting the attraction for now, we begin with the action $\mathcal{S} = \mathcal{S}_{\text{MF}} + \mathcal{S}_{\text{Cooper}}$, where \mathcal{S}_{MF} is the quadratic action corresponding to the solution of the variational procedure, and $\mathcal{S}_{\text{Cooper}} = \int d^2\mathbf{x} \sum_{\tau\sigma} c_{\tau\sigma}^\dagger c_{\bar{\tau}\bar{\sigma}}^\dagger \left[\frac{U_C}{2} c_{\bar{\tau}\bar{\sigma}} c_{\tau\sigma} - (U_\delta + |g_1|) c_{\bar{\tau}\bar{\sigma}} c_{\tau\sigma} \right]$ is the interaction in Eq. (3) restricted to the $\Delta_{\tau\sigma}$ Cooper channel. Following the standard RG procedure [28, 38], we find the flow of the coupling constant V as a function of the energy cutoff Λ . The initial conditions are $\Lambda_0 = W$, and $V_0 = \frac{U_C}{2} - (U_\delta + |g_1|)$. Notice that the secondary

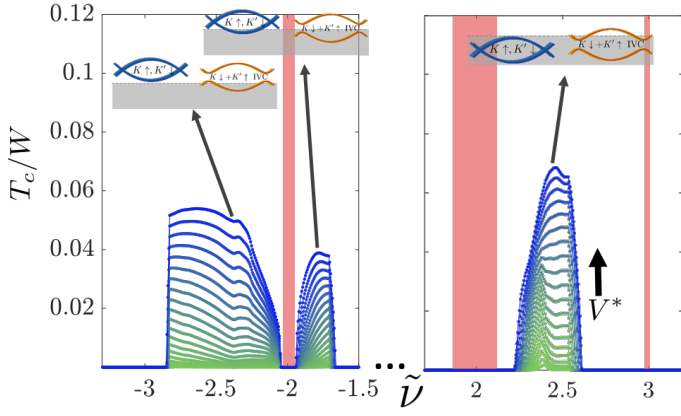


FIG. 3. Superconducting T_c enhancement with increasing retarded attraction V^* near representative fillings. We used the same parameters as in Fig. 1, with $V^* \in [0.12, 0.32] W$, in steps of $0.01W$. Incompressibility regions are demarcated in red. The direction of increased V^* is indicated, as well as the schematic mean-field states from which superconductivity emerges.

interactions *enhance* pairing in this channel whereas the Coulomb repulsion suppresses it.

We now address the role of the acoustic phonon branch mediating the retarded attraction. We observe that due to folding of the acoustic phonon spectrum into the mBZ [39, 40], one should also take into account the “pseudo-optical” branches that are generated. Consequently, the RG equation for the superconductivity coupling constant is [28]

$$\frac{d}{d\Lambda} V = \frac{\mathcal{N}(\Lambda)}{\Lambda} V^2 + \frac{V^*}{W}, \quad (6)$$

where the conventional RG flow in the Cooper channel yields the first term, with $\mathcal{N}(\Lambda)$ being the electronic DOS. The non-standard second term appears because as we lower the energy cutoff, more phonon modes become attractive, we denote their total contribution by V^* , see SM, Sec. S.4.

We use Eq. (6), in conjunction with the variational mean-field results, to find T_c , which we extract as the scale at which the coupling constant becomes comparable with the bandwidth, $|V(T_c)| = W$, signaling its divergence. Notice that because W is the scale at which retarded phonons begin to contribute, at a given V^* and V_0 , Eq. (6) may lead to a critical W , *below which* superconductivity is lost. This is due to the retardation being ineffective in changing the sign of V along the shorter RG flow. Fig. 3 tracks the evolution of several superconducting domes with increasing phonon-mediated attraction V^* .

To take into account the effects of superconducting phase fluctuations on transport, which may be significant in our model as T_c and T_F become comparable, we use the Halperin-Nelson formula to calculate the resistance, see SM Sec. S.5 [28, 41]. The difference between the mean-field T_c and the BKT temperature can be parameterized by $T_{\text{BKT}} = T_c / (1 + \tau_c)$, where $\tau_c \approx T_c / T_F$. Experimental estimates [3] of $\tau_c \sim 0.05 - 0.1$ in MATBG are in qualitative agreement with the values obtained for T_c and T_F with the presented

model [see SM, (S.5)], where we find τ_c in a similar range on the hole side of Fig. 1, and τ_c reaching up to ~ 0.3 on the electron side. Non-zero Δ_{IVC}^\pm in the normal state modifies the dispersion and enables an appreciable Fermi-level DOS even at minuscule fillings. It thus contributes to increasing T_c/T_F as compared to what might be expected from a Dirac-like dispersion.

Fig. 1 features three areas of superconductivity on the hole side. The most prominent one occurs at $\tilde{\nu} = -2 - \epsilon$, adjacent to the $\tilde{\nu} = -2$ IVC phase. In this regime, the gap in the IVC sector is gradually closed with decreasing $\tilde{\nu}$, until it vanishes. The suppression in superconductivity near $\tilde{\nu} \approx -3$ occurs due to flavor-polarization in this sector, similar to those observed in Fig. 2. Superconductivity at this filling is the most robust in experiments, and is routinely observed near fillings of $|\nu| \approx 2 + \epsilon$, often with similar double-hump shape [3]. This shape is due to the two-step process, where first the IVC gap gradually closes when doping away from the IVC, and then two gapless flavors get populated. A similar, but narrower and higher dome appears in our model at $\tilde{\nu} = 2 + \epsilon$. This is because the electron side in our model has larger DOS leading to stronger effective repulsion and wider regions with flavor-polarization. On the other hand, without polarization the larger DOS leads to higher T_c .

A second less dominant superconducting feature observed in some experiments happens near $|\nu| = 2 - \epsilon$, and is also manifest in our model at $\tilde{\nu} = -2 + \epsilon$. Its existence is due to the depolarization of the two non-IVC flavors when $\tilde{\nu}$ is decreased (see SM, Fig. S1), occurring due to the drop in DOS near the band edge. Thus, this feature is sensitive to the details of the flat-band dispersion, possibly explaining its haphazard occurrence.

Lastly, we find superconductivity near the CNP, which has been observed in a few experiments [6], but not often. In essence, it is a modified copy of the $\tilde{\nu} = -2 - \epsilon$ dome, with two flavors participating in the pairing, and the other two forming a gapped IVC state. It has an electron-side counterpart, too.

Discussion.— We have presented a simple phenomenological model which exhibits the key features of MATBG, namely interaction-induced CIs at integer fillings, flavor-symmetry-breaking phase transitions, and robust superconductivity. Though we neglect several ingredients known to be found in MATBG, i.e., long-range Coulomb interactions, intricate wave-functions, fragile topology, and the filling-dependent band-structure, much of the phenomenology is remarkably reproduced. Our minimalistic description of the system’s degrees of freedom, as well as the hierarchy of the interaction energy scales, help to comprehend the experimental phase diagram and its variations between different samples.

The model incorporates two important effects of the twist-induced moiré lattice. First, generation of a flat-band dispersion, with greatly enhanced DOS [1]. Second, a dramatic increase of the electron-phonon coupling [18]. The large DOS enhances the effects of both electron-electron repulsion and the effective phonon-mediated attraction. Here, we use a mean-field approach combined with RG method to study the interplay between the two. Within this paradigm, one ex-

pects that the CIs and superconducting states are in competition with one another. This is indeed consistent with experiments where the strength of the Coulomb interaction is tuned by manipulating the screening environment [5, 15, 16]. Another side-effect of the interplay between Coulomb repulsion and superconductivity is spontaneous spin-valley locking, e.g., near $\nu = -2 - \epsilon$, that may be weakly sensitive to parallel in-plane magnetic fields, leading to a superconducting order parameter with appreciable spin-triplet pairing correlations.

It is worth noting the discrepancies between our simplified model and experimental observations. In most experiments, the phase at charge neutrality appears to be semi-metallic (though there are notable exceptions). Here, we find the strongest CI at this filling. Furthermore, we find that an insulator at $|\nu| = 3$ is accompanied by an insulator at $|\nu| = 1$, which is seldom seen in experiments. One possible cause is a modification of the band-structure itself as more electrons enter the system. It has been argued [42–45] that the flat bands are least flat near charge-neutrality, which may explain the empirical scarcity of insulators at low fillings. Another possibility is that the semi-metallic phase at the CNP is promoted by strain [46]. These effects are not considered in this work. Moreover, there is convincing experimental evidence [47, 48] that flavor-fluctuations near $|\nu| = 1$ are non-negligible, suggesting one should include spin and valley fluctuations to fully understand this region of the phase diagram.

Disorder has also yet to be explored in this model. As was suggested [49], it may settle the discrepancy regarding the insulator at charge neutrality, as well as the possible absence of a quantized transverse response when CIs occur at odd integer fillings. The framework we proposed can help elucidate

the roles of both fluctuations (by treating our phase diagram as a saddle-point around which fluctuations occur) and disorder effects (by quantifying the competition between different phases and taking into account the effect of disorder on this competition).

Our model may be used to investigate additional superconducting channels, e.g., d-wave [17], and explore under what conditions they become dominant. Furthermore, this scheme, albeit with different interactions, single-particle terms, DOS, or number of flavors, may be applicable to other moiré platforms which display similar correlation-induced symmetry-breaking phenomena, such as ABC-stacked trilayer graphene on top of hexagonal boron-nitride (hBN) [50], twisted double-bilayer graphene [51, 52], MATBG aligned with hBN [53, 54] (where we can account for the absence of superconductivity, SM Sec. S.6), and magic-angle twisted trilayer graphene [55, 56].

ACKNOWLEDGMENTS

We acknowledge enlightening discussions with Pablo Jarillo-Herrero, Shahal Ilani, Uri Zondiner, Ohad Antebi, and Keshav Pareek. This project was partially supported by grants from the ERC under the European Union’s Horizon 2020 research and innovation programme (grant agreements LEGOTOP No. 788715 and HQMAT No. 817799), the DFG (CRC/Transregio 183, EI 519/7-1), the BSF and NSF (2018643), the ISF Quantum Science and Technology (2074/19), and a research grant from Irving and Cherna Moskowitz.

-
- [1] R. Bistritzer and A. H. MacDonald, Moiré bands in twisted double-layer graphene, *Proceedings of the National Academy of Sciences* **108**, 12233 (2011), <https://www.pnas.org/content/108/30/12233.full.pdf>.
 - [2] Y. Cao, V. Fatemi, A. Demir, S. Fang, S. L. Tomarken, J. Y. Luo, J. D. Sanchez-Yamagishi, K. Watanabe, T. Taniguchi, E. Kaxiras, R. C. Ashoori, and P. Jarillo-Herrero, Correlated insulator behaviour at half-filling in magic-angle graphene superlattices, *Nature* **556**, 80 (2018).
 - [3] Y. Cao, V. Fatemi, S. Fang, K. Watanabe, T. Taniguchi, E. Kaxiras, and P. Jarillo-Herrero, Unconventional superconductivity in magic-angle graphene superlattices, *Nature* **556**, 43 (2018).
 - [4] M. Yankowitz, S. Chen, H. Polshyn, Y. Zhang, K. Watanabe, T. Taniguchi, D. Graf, A. F. Young, and C. R. Dean, Tuning superconductivity in twisted bilayer graphene, *Science* **363**, 1059 (2019), <https://science.sciencemag.org/content/363/6431/1059.full.pdf>.
 - [5] Y. Saito, J. Ge, K. Watanabe, T. Taniguchi, and A. F. Young, Independent superconductors and correlated insulators in twisted bilayer graphene, *Nature Physics* **16**, 926 (2020).
 - [6] X. Lu, P. Stepanov, W. Yang, M. Xie, M. A. Aamir, I. Das, C. Urgell, K. Watanabe, T. Taniguchi, G. Zhang, A. Bachtold, A. H. MacDonald, and D. K. Efetov, Superconductors, orbital magnets and correlated states in magic-angle bilayer graphene, *Nature* **574**, 653 (2019).
 - [7] H. C. Po, L. Zou, A. Vishwanath, and T. Senthil, Origin of mott insulating behavior and superconductivity in twisted bilayer graphene, *Phys. Rev. X* **8**, 031089 (2018).
 - [8] J. F. Dodaro, S. A. Kivelson, Y. Schattner, X. Q. Sun, and C. Wang, Phases of a phenomenological model of twisted bilayer graphene, *Phys. Rev. B* **98**, 075154 (2018).
 - [9] J. Kang and O. Vafek, Strong coupling phases of partially filled twisted bilayer graphene narrow bands, *Phys. Rev. Lett.* **122**, 246401 (2019).
 - [10] N. Bultinck, E. Khalaf, S. Liu, S. Chatterjee, A. Vishwanath, and M. P. Zaletel, Ground state and hidden symmetry of magic-angle graphene at even integer filling, *Phys. Rev. X* **10**, 031034 (2020).
 - [11] J. Kang and O. Vafek, Non-abelian dirac node braiding and near-degeneracy of correlated phases at odd integer filling in magic-angle twisted bilayer graphene, *Phys. Rev. B* **102**, 035161 (2020).
 - [12] O. Vafek and J. Kang, Renormalization group study of hidden symmetry in twisted bilayer graphene with coulomb interactions, *Phys. Rev. Lett.* **125**, 257602 (2020).
 - [13] B. Lian, Z.-D. Song, N. Regnault, D. K. Efetov, A. Yazdani, and B. A. Bernevig, Twisted bilayer graphene. iv. exact insulator ground states and phase diagram, *Phys. Rev. B* **103**, 205414 (2021).

- (2021).
- [14] F. Xie, A. Cowsik, Z.-D. Song, B. Lian, B. A. Bernevig, and N. Regnault, Twisted bilayer graphene. vi. an exact diagonalization study at nonzero integer filling, *Phys. Rev. B* **103**, 205416 (2021).
 - [15] P. Stepanov, I. Das, X. Lu, A. Fahimniya, K. Watanabe, T. Taniguchi, F. H. L. Koppens, J. Lischner, L. Levitov, and D. K. Efetov, Untying the insulating and superconducting orders in magic-angle graphene, *Nature* **583**, 375 (2020).
 - [16] X. Liu, Z. Wang, K. Watanabe, T. Taniguchi, O. Vafek, and J. I. A. Li, Tuning electron correlation in magic-angle twisted bilayer graphene using coulomb screening (2020), [arXiv:2003.11072](https://arxiv.org/abs/2003.11072).
 - [17] F. Wu, A. H. MacDonald, and I. Martin, Theory of phonon-mediated superconductivity in twisted bilayer graphene, *Phys. Rev. Lett.* **121**, 257001 (2018).
 - [18] B. Lian, Z. Wang, and B. A. Bernevig, Twisted bilayer graphene: A phonon-driven superconductor, *Phys. Rev. Lett.* **122**, 257002 (2019).
 - [19] F. Wu, E. Hwang, and S. Das Sarma, Phonon-induced giant linear-in- T resistivity in magic angle twisted bilayer graphene: Ordinary strangeness and exotic superconductivity, *Phys. Rev. B* **99**, 165112 (2019).
 - [20] B. A. Bernevig, B. Lian, A. Cowsik, F. Xie, N. Regnault, and Z.-D. Song, Twisted bilayer graphene. v. exact analytic many-body excitations in coulomb hamiltonians: Charge gap, goldstone modes, and absence of cooper pairing, *Phys. Rev. B* **103**, 205415 (2021).
 - [21] C. Lewandowski, D. Chowdhury, and J. Ruhman, Pairing in magic-angle twisted bilayer graphene: Role of phonon and plasmon umklapp, *Phys. Rev. B* **103**, 235401 (2021).
 - [22] D. Wong, K. P. Nuckolls, M. Oh, B. Lian, Y. Xie, S. Jeon, K. Watanabe, T. Taniguchi, B. A. Bernevig, and A. Yazdani, Cascade of electronic transitions in magic-angle twisted bilayer graphene, *Nature* **582**, 198 (2020).
 - [23] U. Zondiner, A. Rozen, D. Rodan-Legrain, Y. Cao, R. Queiroz, T. Taniguchi, K. Watanabe, Y. Oreg, F. von Oppen, A. Stern, E. Berg, P. Jarillo-Herrero, and S. Ilani, Cascade of phase transitions and dirac revivals in magic-angle graphene, *Nature* **582**, 203 (2020).
 - [24] J. Kang, B. A. Bernevig, and O. Vafek, Cascades between light and heavy fermions in the normal state of magic angle twisted bilayer graphene (2021), [arXiv:2104.01145 \[cond-mat.str-el\]](https://arxiv.org/abs/2104.01145).
 - [25] V. V. Tolmachev, Logarithmic criterion for superconductivity, *SPhD* **6**, 800 (1962).
 - [26] P. Morel and P. W. Anderson, Calculation of the superconducting state parameters with retarded electron-phonon interaction, *Phys. Rev.* **125**, 1263 (1962).
 - [27] The single-particle term in the Hamiltonian we use is not C_3 -symmetric, unlike the MATBG dispersion. However, within this model it has little consequence, as we also do not explore spontaneous C_3 symmetry breaking.
 - [28] See Supplemental Material for details regarding the single-particle Hamiltonian, the variational mean-field approach, calculation of $\tilde{\nu}$, the superconducting RG equation, the role of superconducting phase fluctuations, and suppression of superconductivity by alignment with h-BN, which includes Refs. [57–63].
 - [29] It can be directly checked for example that $(\Psi^\dagger C_3 \vec{\partial}_\alpha C_3^\dagger \Psi)^2 = (\Psi^\dagger \vec{\partial}_\alpha \Psi)$ for $\alpha = 1, \dots, 4$.
 - [30] N. Bultinck, S. Chatterjee, and M. P. Zaletel, Mechanism for anomalous hall ferromagnetism in twisted bilayer graphene, *Phys. Rev. Lett.* **124**, 166601 (2020).
 - [31] K. Nomura and A. H. MacDonald, Quantum hall ferromagnetism in graphene, *Phys. Rev. Lett.* **96**, 256602 (2006).
 - [32] M. Kharitonov, Phase diagram for the $\nu = 0$ quantum hall state in monolayer graphene, *Phys. Rev. B* **85**, 155439 (2012).
 - [33] J. S. Hofmann, E. Khalaf, A. Vishwanath, E. Berg, and J. Y. Lee, Fermionic monte carlo study of a realistic model of twisted bilayer graphene (2021), [arXiv:2105.12112 \[cond-mat.str-el\]](https://arxiv.org/abs/2105.12112).
 - [34] B. T. Zhou, N. F. Q. Yuan, H.-L. Jiang, and K. T. Law, Ising superconductivity and majorana fermions in transition-metal dichalcogenides, *Phys. Rev. B* **93**, 180501 (2016).
 - [35] A. M. Clogston, Upper limit for the critical field in hard superconductors, *Phys. Rev. Lett.* **9**, 266 (1962).
 - [36] J. M. Lu, O. Zheliuk, I. Leermakers, N. F. Q. Yuan, U. Zeitler, K. T. Law, and J. T. Ye, Evidence for two-dimensional ising superconductivity in gated mos2, *Science* **350**, 1353 (2015), <https://science.sciencemag.org/content/350/6266/1353.full.pdf>.
 - [37] X. Xi, Z. Wang, W. Zhao, J.-H. Park, K. T. Law, H. Berger, L. Forró, J. Shan, and K. F. Mak, Ising pairing in superconducting nbse2 atomic layers, *Nature Physics* **12**, 139 (2016).
 - [38] N. Nagaosa, *Quantum field theory in condensed matter physics* (Springer Science & Business Media, 1999).
 - [39] T. Cea and F. Guinea, Coulomb interaction, phonons, and superconductivity in twisted bilayer graphene (2021), [arXiv:2103.01815 \[cond-mat.str-el\]](https://arxiv.org/abs/2103.01815).
 - [40] A. I. Cocemasov, D. L. Nika, and A. A. Balandin, Phonons in twisted bilayer graphene, *Phys. Rev. B* **88**, 035428 (2013).
 - [41] B. I. Halperin and D. R. Nelson, Resistive transition in superconducting films, *Journal of Low Temperature Physics* **36**, 599 (1979).
 - [42] M. J. Calderón and E. Bascones, Interactions in the 8-orbital model for twisted bilayer graphene, *Phys. Rev. B* **102**, 155149 (2020).
 - [43] Z. A. H. Goodwin, V. Vitale, X. Liang, A. A. Mostofi, and J. Lischner, Hartree theory calculations of quasiparticle properties in twisted bilayer graphene (2020), [arXiv:2004.14784](https://arxiv.org/abs/2004.14784).
 - [44] M. Xie and A. H. MacDonald, Weak-field hall resistivity and spin/valley flavor symmetry breaking in matbg (2020), [arXiv:2010.07928](https://arxiv.org/abs/2010.07928).
 - [45] C. Lewandowski, S. Nadj-Perge, and D. Chowdhury, Does filling-dependent band renormalization aid pairing in twisted bilayer graphene? (2021), [arXiv:2102.05661](https://arxiv.org/abs/2102.05661).
 - [46] D. E. Parker, T. Soejima, J. Hauschild, M. P. Zaletel, and N. Bultinck, Strain-induced quantum phase transitions in magic angle graphene (2020), [arXiv:2012.09885 \[cond-mat.str-el\]](https://arxiv.org/abs/2012.09885).
 - [47] Y. Saito, F. Yang, J. Ge, X. Liu, K. Watanabe, T. Taniguchi, J. I. A. Li, E. Berg, and A. F. Young, Isospin pomeranchuk effect and the entropy of collective excitations in twisted bilayer graphene (2020), [arXiv:2008.10830](https://arxiv.org/abs/2008.10830).
 - [48] A. Rozen, J. M. Park, U. Zondiner, Y. Cao, D. Rodan-Legrain, T. Taniguchi, K. Watanabe, Y. Oreg, A. Stern, E. Berg, P. Jarillo-Herrero, and S. Ilani, Entropic evidence for a pomeranchuk effect in magic angle graphene (2020), [arXiv:2009.01836](https://arxiv.org/abs/2009.01836).
 - [49] A. Thomson and J. Alicea, Recovery of massless dirac fermions at charge neutrality in strongly interacting twisted bilayer graphene with disorder, *Phys. Rev. B* **103**, 125138 (2021).
 - [50] G. Chen, L. Jiang, S. Wu, B. Lyu, H. Li, B. L. Chittari, K. Watanabe, T. Taniguchi, Z. Shi, J. Jung, Y. Zhang, and F. Wang, Evidence of a gate-tunable mott insulator in a trilayer graphene moiré superlattice, *Nature Physics* **15**, 237 (2019).
 - [51] M. He, Y. Li, J. Cai, Y. Liu, K. Watanabe, T. Taniguchi, X. Xu, and M. Yankowitz, Symmetry breaking in twisted double bilayer graphene, *Nature Physics* **17**, 26 (2021).
 - [52] C. Shen, Y. Chu, Q. Wu, N. Li, S. Wang, Y. Zhao, J. Tang,

- J. Liu, J. Tian, K. Watanabe, T. Taniguchi, R. Yang, Z. Y. Meng, D. Shi, O. V. Yazyev, and G. Zhang, Correlated states in twisted double bilayer graphene, *Nature Physics* **16**, 520 (2020).
- [53] G. Chen, A. L. Sharpe, E. J. Fox, Y.-H. Zhang, S. Wang, L. Jiang, B. Lyu, H. Li, K. Watanabe, T. Taniguchi, Z. Shi, T. Senthil, D. Goldhaber-Gordon, Y. Zhang, and F. Wang, Tunable correlated Chern insulator and ferromagnetism in a moiré superlattice, *Nature* **579**, 56 (2020).
- [54] M. Serlin, C. L. Tschirhart, H. Polshyn, Y. Zhang, J. Zhu, K. Watanabe, T. Taniguchi, L. Balents, and A. F. Young, Intrinsic quantized anomalous Hall effect in a moiré heterostructure, *Science* **367**, 900 (2020), <https://science.sciencemag.org/content/367/6480/900.full.pdf>.
- [55] J. M. Park, Y. Cao, K. Watanabe, T. Taniguchi, and P. Jarillo-Herrero, Tunable phase boundaries and ultra-strong coupling superconductivity in mirror symmetric magic-angle trilayer graphene (2020), [arXiv:2012.01434](https://arxiv.org/abs/2012.01434).
- [56] Z. Hao, A. M. Zimmerman, P. Ledwith, E. Khalaf, D. H. Najafabadi, K. Watanabe, T. Taniguchi, A. Vishwanath, and P. Kim, Electric field tunable unconventional superconductivity in alternating twist magic-angle trilayer graphene (2020), [arXiv:2012.02773](https://arxiv.org/abs/2012.02773).
- [57] P. B. Allen and R. C. Dynes, Transition temperature of strong-coupled superconductors reanalyzed, *Phys. Rev. B* **12**, 905 (1975).
- [58] N. B. Kopnin and E. B. Sonin, Bcs superconductivity of Dirac electrons in graphene layers, *Phys. Rev. Lett.* **100**, 246808 (2008).
- [59] A. Abrikosov, *Fundamentals of the Theory of Metals* (Dover Publications, 2017).
- [60] L. Aslamasov and A. Larkin, The influence of fluctuation pairing of electrons on the conductivity of normal metal, *Physics Letters A* **26**, 238 (1968).
- [61] H. Kim, N. Leconte, B. L. Chittari, K. Watanabe, T. Taniguchi, A. H. MacDonald, J. Jung, and S. Jung, Accurate gap determination in monolayer and bilayer graphene/h-bn moiré superlattices, *Nano Letters* **18**, 7732 (2018), pMID: 30457338, <https://doi.org/10.1021/acs.nanolett.8b03423>.
- [62] H. Aker, A. H. MacDonald, S. M. Girvin, and M. R. Norman, Vortex-lattice states at strong magnetic fields, *Phys. Rev. Lett.* **67**, 2375 (1991).
- [63] K. Maki, Gapless superconductivity, *Superconductivity: Part 2* (1969).

SUPPLEMENTAL MATERIAL

S.1. THE PROPOSED MODEL AND MEAN-FIELD VARIATIONAL APPROACH

A. Model description

In this work we explore a model comprised of eight flat bands with valley (K/K'), spin, and sublattice (A/B) degrees of freedom, labeled by Pauli matrices τ_i , s_i , and σ_i , respectively. This choice of basis is motivated by the MATBG sublattice-polarized basis which adiabatically connects the fully-polarized bands in the chiral limit to the realistic model [10]. These bands have a valley-dependent Chern number, $C = \sigma_z \tau_z$, which can be understood from the two chiral Dirac points in each valley. Using the 8-spinor

$$\Psi = (c_{K\uparrow A}, c_{K\uparrow B}, c_{K'\uparrow A}, c_{K'\uparrow B}, c_{K\downarrow A}, c_{K\downarrow B}, c_{K'\downarrow A}, c_{K'\downarrow B})^T, \quad (\text{S1})$$

We write the Hamiltonian as

$$H = \sum_{\mathbf{k}} \Psi_{\mathbf{k}}^\dagger h_0(\mathbf{k}) \Psi_{\mathbf{k}} + H_{\text{int}}, \quad (\text{S2})$$

where the single-particle part is of the form

$$h_0(\mathbf{k}) = f_x(\mathbf{k}) \sigma_x + f_y(\mathbf{k}) \sigma_y \tau_z + f_{p-h}(\mathbf{k}). \quad (\text{S3})$$

In this work, we use

$$f_x(\mathbf{k}) = \frac{1}{2M_{\text{eff}}} [k_x^2 - k_y^2 - \tilde{k}^2], \quad (\text{S4})$$

$$f_y(\mathbf{k}) = \frac{1}{2M_{\text{eff}}} [2k_x k_y], \quad (\text{S5})$$

and work in units where $2M_{\text{eff}} = 1$ for convenience. This produces an energy spectrum with two Dirac cones of the same chirality at momenta $(k_x, k_y) = (\pm \tilde{k}, 0)$, allowing us to emulate the structure of the isolated flat bands in magic angle twisted bilayer graphene (MATBG), including the same topological structure of Chern bands once a perturbation $\propto \sigma_z$ is introduced, opening a band gap. The limits of our effective Brillouin are $k_x \in [-0.56, 0.56]$ and $k_y \in [-0.26, 0.26]$. We also use $\tilde{k} = 0.5$.

The last term in the single-particle part of the Hamiltonian introduces particle-hole asymmetry into the model. In the case of a single Dirac cone with a spectrum $\propto \pm |\mathbf{k}|$, the simplest way to include particle hole asymmetry is to add a quadratic term $\propto |\mathbf{k}|^2$ which induces curvature in the Dirac dispersion. Since we wish to introduce such a curvature near *both* the Dirac points, we choose to use

$$f_{p-h}(\mathbf{k}) = \frac{1}{2m_{p-h}} \sqrt{(k_x - \tilde{k})^2 + k_y^2} \sqrt{(k_x + \tilde{k})^2 + k_y^2}, \quad (\text{S6})$$

which indeed has the desired effect on the electronic density of states, see Fig. S1. Eq. (S6) has spurious singularities at the Dirac points. We have checked that our results do not change qualitatively if we use different forms of the particle-hole symmetry breaking term, as long as the overall DOS remains similar. Since experimental evidence suggest the conduction band is flatter as compared to the valence band [4, 23, 44], we choose the sign of f_{p-h} to be negative throughout the mBZ. Throughout our calculations $m_{p-h} = -2.4$ is used

We stress that the specific details of $h_0(\mathbf{k})$ are not important within our phenomenological model, where due to the mean-field nature of our treatment and the locality of the interactions, only the DOS is important in determining the phase diagram.

We define the combined bandwidth of the conduction and valence bands of the single-particle Hamiltonian h_0 as W . This energy scale is our reference point to which we compare interaction energies, transition temperatures and gap sizes.

The interaction part of the Hamiltonian can be written out as a sum of four contributions,

$$\begin{aligned} H_{\text{int}} = & \frac{U_C}{2\Omega} \sum_{\mathbf{k}, \mathbf{k}', \mathbf{q}} \Psi_{\mathbf{k}+\mathbf{q}}^\dagger \Psi_{\mathbf{k}} \Psi_{\mathbf{k}'-\mathbf{q}}^\dagger \Psi_{\mathbf{k}'} \\ & + \frac{U_\delta}{2\Omega} \sum_{\mathbf{k}, \mathbf{k}', \mathbf{q}} \left[\Psi_{\mathbf{k}+\mathbf{q}}^\dagger \sigma_x \tau_z \Psi_{\mathbf{k}} \Psi_{\mathbf{k}'-\mathbf{q}}^\dagger \sigma_x \tau_z \Psi_{\mathbf{k}'} + \Psi_{\mathbf{k}+\mathbf{q}}^\dagger \sigma_y \Psi_{\mathbf{k}} \Psi_{\mathbf{k}'-\mathbf{q}}^\dagger \sigma_y \Psi_{\mathbf{k}'} \right] \\ & + \frac{|g_1|}{2\Omega} \sum_{\mathbf{k}, \mathbf{k}', \mathbf{q}} \left[\Psi_{\mathbf{k}+\mathbf{q}}^\dagger \sigma_y \tau_z \Psi_{\mathbf{k}} \Psi_{\mathbf{k}'-\mathbf{q}}^\dagger \sigma_y \tau_z \Psi_{\mathbf{k}'} + \Psi_{\mathbf{k}+\mathbf{q}}^\dagger \sigma_x \Psi_{\mathbf{k}} \Psi_{\mathbf{k}'-\mathbf{q}}^\dagger \sigma_x \Psi_{\mathbf{k}'} \right] \\ & + \frac{|g_2|}{2\Omega} \sum_{\mathbf{k}, \mathbf{k}', \mathbf{q}} \left[\Psi_{\mathbf{k}+\mathbf{q}}^\dagger \sigma_x \tau_x \Psi_{\mathbf{k}} \Psi_{\mathbf{k}'-\mathbf{q}}^\dagger \sigma_x \tau_x \Psi_{\mathbf{k}'} + \Psi_{\mathbf{k}+\mathbf{q}}^\dagger \sigma_x \tau_y \Psi_{\mathbf{k}} \Psi_{\mathbf{k}'-\mathbf{q}}^\dagger \sigma_x \tau_y \Psi_{\mathbf{k}'} \right]. \end{aligned} \quad (\text{S7})$$

Let us briefly discuss the origin of each of the terms in H_{int} . The first and most dominant U_C term, is the ‘‘symmetric’’ or structure-less density-density interaction due to the short range part of the screened Coulomb interaction. The second sub-dominant term U_δ has unusual structure in valley-sublattice space. It represents the part of the flat-band-projected Coulomb interactions which anti-commute with the chirality operator σ_z . As discussed in Ref. [10], its structure is constrained by the symmetries of MATBG.

The next two terms, proportional to g_1 and g_2 , originate in electron-phonon interactions. The relevant phonons here are the *optical* in-plane phonons of monolayer graphene. Due to their high frequency, they lead to effective instantaneous electron-electron interactions. The structure of the interactions in valley-sublattice space is inherited from the structure of the electron-phonon couplings of the relevant modes. More concretely, g_1 terms are due to coupling of phonons with zero momentum, whereas g_2 originates in coupling to phonon branches located near the K and K' points of the monolayer graphene Brillouin zone. Thus, the g_2 interactions contain inter-valley scattering (τ_x/τ_y elements), whereas g_1 interactions are strictly intra-valley in nature.

B. Variational mean-field approach

We begin by making an ansatz for a mean-field quadratic Hamiltonian

$$H_{\text{MF}} = \sum_{\mathbf{k}} \Psi_{\mathbf{k}}^\dagger h_{\text{MF}}(\mathbf{k}) \Psi_{\mathbf{k}} = \sum_{\mathbf{k}, \lambda} \xi_{\mathbf{k}, \lambda} \psi_{\mathbf{k}, \lambda}^\dagger \psi_{\mathbf{k}, \lambda}, \quad (\text{S8})$$

where we have written H_{MF} in a new diagonal basis on the right hand side, with $\psi_{\mathbf{k}, \lambda}$ a fermionic annihilation operator with momentum \mathbf{k} , and λ labels the eight eigenstates per \mathbf{k} . Expectation values calculated within the distribution generated by H_{MF} follow

$$\left\langle \psi_{\mathbf{k}, \lambda}^\dagger \psi_{\mathbf{k}', \lambda'} \right\rangle_{\text{MF}} = \delta_{\mathbf{k}, \mathbf{k}'} \delta_{\lambda, \lambda'} f(\beta \xi_{\mathbf{k}, \lambda}), \quad (\text{S9})$$

with $f(x) = (1 + e^x)^{-1}$ the Fermi-Dirac distribution, and β is the inverse temperature.

Our aim is to find the mean-field ansatz which minimizes the grand potential

$$\Phi = \langle H - \mu N \rangle_{\text{MF}} - T \sum_{\mathbf{k}, \lambda} \ln \left(1 + e^{-\beta |\xi_{\mathbf{k}, \lambda}|} \right), \quad (\text{S10})$$

with $N = \sum_{\mathbf{k}} \Psi_{\mathbf{k}}^{\dagger} \Psi_{\mathbf{k}} = \sum_{\mathbf{k}, \lambda} \psi_{\mathbf{k}, \lambda}^{\dagger} \psi_{\mathbf{k}, \lambda}$ the particle number operator, and μ the chemical potential.

The only non-quadratic part in the evaluation of Eq. (S10) is $\langle H_{\text{int}} \rangle_{\text{MF}}$, for which we can employ Wick's theorem since H_{MF} is quadratic in fermion operators. Beginning with the dominant “structure-less” term, $H_{\text{int}, \text{C}} = \frac{U_{\text{C}}}{2\Omega} \sum_{\mathbf{k}, \mathbf{k}', \mathbf{q}} \Psi_{\mathbf{k}+\mathbf{q}}^{\dagger} \Psi_{\mathbf{k}} \Psi_{\mathbf{k}'-\mathbf{q}}^{\dagger} \Psi_{\mathbf{k}'}$, we find (we omit the MF subscript from $\langle \cdot \rangle_{\text{MF}}$ for simplicity henceforth)

$$\begin{aligned} \frac{\langle H_{\text{int}, \text{C}} \rangle}{\Omega} &= \frac{U_{\text{C}}}{2\Omega^2} \sum_{\mathbf{k}, \mathbf{k}', \mathbf{q}} \sum_{\tau' s' \sigma'} \sum_{\tau s \sigma} \left\langle c_{\tau s \sigma}^{\dagger}(\mathbf{k} + \mathbf{q}) c_{\tau s \sigma}(\mathbf{k}) c_{\tau' s' \sigma'}^{\dagger}(\mathbf{k}' - \mathbf{q}) c_{\tau' s' \sigma'}(\mathbf{k}') \right\rangle \\ &= \frac{U_{\text{C}}}{2} \left[\sum_{\mathbf{k}, \tau s \sigma} \langle c_{\tau s \sigma}^{\dagger}(\mathbf{k}) c_{\tau s \sigma}(\mathbf{k}) \rangle \right]^2 \\ &\quad + \frac{U_{\text{C}}}{2} \sum_{\tau s \sigma} \left[\frac{1}{\Omega} \sum_{\mathbf{k}} \langle c_{\tau s \sigma}^{\dagger}(\mathbf{k}) c_{\tau s \sigma}(\mathbf{k}) \rangle \right] \left[\frac{1}{\Omega} \sum_{\mathbf{k}'} \langle 1 - c_{\tau s \sigma}^{\dagger}(\mathbf{k}') c_{\tau s \sigma}(\mathbf{k}') \rangle \right] \\ &\quad - \frac{U_{\text{C}}}{2} \sum_{\tau s \sigma} \left| \frac{1}{\Omega} \sum_{\mathbf{k}} \langle c_{\tau s \sigma}^{\dagger}(\mathbf{k}') c_{\tau s \sigma}(\mathbf{k}') \rangle \right|^2 \\ &\quad - \frac{U_{\text{C}}}{2} \sum_{\tau s \sigma s'} \left| \frac{1}{\Omega} \sum_{\mathbf{k}} \langle c_{\tau s \sigma}^{\dagger}(\mathbf{k}) c_{\bar{\tau} s' \bar{\sigma}}(\mathbf{k}) \rangle \right|^2. \end{aligned} \quad (\text{S11})$$

The second to last term vanishes due to the chirality of the single-particle Hamiltonian, such that summation over the entire Brillouin zone of the term $\langle c_{\tau s A}^{\dagger}(\mathbf{k}) c_{\tau s B}(\mathbf{k}) \rangle$ is zero. The first two terms in Eq. (S11) may lead to generalized Stoner instabilities, given U_{C} is sufficiently strong as compared to the bandwidth.

The last term indicates that this interaction terms also favors the formation of any inter-valley coherent (IVC) order. This order may be understood as a sort of Stoner instability as well, where the valley U_{v} (1) symmetry is spontaneously broken. We have also implicitly assumed the absence of any IVC order between two bands with opposite Chern numbers $C = \sigma_z \tau_z$, as such orders are prohibited from being uniform in \mathbf{k} . Instead, one expects to find an Abrikosov-like vortex lattice structure of this order parameter (reminiscent of intra-Landau-level superconductivity [62]), which comes with great kinetic energy cost [30]. In this work we assume that this energy cost suppresses these kinds of IVC order in the mean-field state.

We follow the same procedure for the secondary interaction terms, and we find ($H_{\text{int}, \delta}$, $H_{\text{int}, \text{ph}, 1}$, and $H_{\text{int}, \text{ph}, 2}$ are the parts of H_{int} proportional to U_{δ} , g_1 , and g_2 , respectively)

$$\begin{aligned} \frac{\langle H_{\text{int}, \delta} \rangle}{\Omega} &= U_{\delta} \sum_{\tau s \sigma} \left[\frac{1}{\Omega} \sum_{\mathbf{k}} \langle c_{\tau s \sigma}^{\dagger}(\mathbf{k}) c_{\tau s \sigma}(\mathbf{k}) \rangle \right] \left[\frac{1}{\Omega} \sum_{\mathbf{k}'} \langle 1 - c_{\tau s \bar{\sigma}}^{\dagger}(\mathbf{k}') c_{\tau s \bar{\sigma}}(\mathbf{k}') \rangle \right] \\ &\quad + U_{\delta} \sum_{\tau s \sigma} \left[\frac{1}{\Omega} \sum_{\mathbf{k}} \langle c_{\tau s \sigma}^{\dagger}(\mathbf{k}) c_{\bar{\tau} s \bar{\sigma}}(\mathbf{k}) \rangle \right] \left[\frac{1}{\Omega} \sum_{\mathbf{k}'} \langle c_{\bar{\tau} s \sigma}^{\dagger}(\mathbf{k}') c_{\tau s \bar{\sigma}}(\mathbf{k}') \rangle \right] \\ &\quad + U_{\delta} \sum_{\tau s \sigma} \left[\frac{1}{\Omega} \sum_{\mathbf{k}} \langle c_{\tau s \sigma}^{\dagger}(\mathbf{k}) c_{\bar{\tau} s \bar{\sigma}}(\mathbf{k}) \rangle \right] \left[\frac{1}{\Omega} \sum_{\mathbf{k}'} \langle c_{\bar{\tau} s \sigma}^{\dagger}(\mathbf{k}') c_{\tau s \bar{\sigma}}(\mathbf{k}') \rangle \right], \end{aligned} \quad (\text{S12})$$

$$\begin{aligned} \frac{\langle H_{\text{int}, \text{ph}, 1} \rangle}{\Omega} &= -|g_1| \sum_{\tau s \sigma} \left[\frac{1}{\Omega} \sum_{\mathbf{k}} \langle c_{\tau s \sigma}^{\dagger}(\mathbf{k}) c_{\tau s \sigma}(\mathbf{k}) \rangle \right] \left[\frac{1}{\Omega} \sum_{\mathbf{k}'} \langle 1 - c_{\tau s \bar{\sigma}}^{\dagger}(\mathbf{k}') c_{\tau s \bar{\sigma}}(\mathbf{k}') \rangle \right] \\ &\quad + |g_1| \sum_{\tau s \sigma} \left[\frac{1}{\Omega} \sum_{\mathbf{k}} \langle c_{\tau s \sigma}^{\dagger}(\mathbf{k}) c_{\bar{\tau} s \bar{\sigma}}(\mathbf{k}) \rangle \right] \left[\frac{1}{\Omega} \sum_{\mathbf{k}'} \langle c_{\bar{\tau} s \sigma}^{\dagger}(\mathbf{k}') c_{\tau s \bar{\sigma}}(\mathbf{k}') \rangle \right] \\ &\quad + |g_1| \sum_{\tau s \sigma} \left[\frac{1}{\Omega} \sum_{\mathbf{k}} \langle c_{\tau s \sigma}^{\dagger}(\mathbf{k}) c_{\bar{\tau} s \bar{\sigma}}(\mathbf{k}) \rangle \right] \left[\frac{1}{\Omega} \sum_{\mathbf{k}'} \langle c_{\bar{\tau} s \sigma}^{\dagger}(\mathbf{k}') c_{\tau s \bar{\sigma}}(\mathbf{k}') \rangle \right], \end{aligned} \quad (\text{S13})$$

$$\begin{aligned} \frac{\langle H_{\text{int,ph},2} \rangle}{\Omega} = & -|g_2| \sum_{\tau s \sigma} \left[\frac{1}{\Omega} \sum_{\mathbf{k}} \langle c_{\tau s \sigma}^\dagger(\mathbf{k}) c_{\tau s \sigma}(\mathbf{k}) \rangle \right] \left[\frac{1}{\Omega} \sum_{\mathbf{k}'} \langle 1 - c_{\bar{\tau} s \bar{\sigma}}^\dagger(\mathbf{k}') c_{\bar{\tau} s \bar{\sigma}}(\mathbf{k}') \rangle \right] \\ & - 2|g_2| \left| \sum_{s \sigma} \frac{1}{\Omega} \sum_{\mathbf{k}} \langle c_{K s \sigma}^\dagger(\mathbf{k}) c_{K' s \bar{\sigma}}(\mathbf{k}) \rangle \right|^2. \end{aligned} \quad (\text{S14})$$

From the first line of Eq. (S12) and the first line of Eq. (S13) we can understand that U_δ suppresses intra-flavor sublattice symmetry breaking (σ_z terms), whereas g_1 promotes such ordered states. This can be understood from examining the sign of the interaction between the mean-field densities of the same spin-valley flavor on opposite sub-lattices.

The second line in both equations addresses opposite-spin IVC orders. It appears both U_δ and g_1 favor IVCs which have $\langle c_{\tau s A}^\dagger c_{\bar{\tau} s' B} \rangle = -\langle c_{\tau s B}^\dagger c_{\bar{\tau} s' A} \rangle$, leading to an order parameter proportional to σ_y . As we see from the last lines in (S12)–(S13), this same statement is true for same-spin IVC.

However, this same-spin IVC order is suppressed due to the last line of Eq. (S14), which favors σ_x alignment within each IVC sector, as well as alignment between the two sectors. In order to avoid this competition, which exists only when one considers same-spin IVC order, we focus our attention on opposite-spin IVC orders.

Moreover, the first line of Eq. (S14) explicitly favors inter-valley antiferromagnetism whenever the spin $SU(2)$ is broken, further bolstering our conclusions regarding the type of IVC one expects this model to favor.

To conclude, analytical examination of the mean-field energetics motivates us to write the variational ansatz Hamiltonian with the following form,

$$H_{\text{MF}} = \sum_{\mathbf{k}} \Psi_{\mathbf{k}}^\dagger \left[h_0(\mathbf{k}) + \begin{pmatrix} \mu_1 + m_1 & & & & & & & \Delta_{\text{ivc}}^+ \\ & \mu_1 - m_1 & & & & & & -\Delta_{\text{ivc}}^+ \\ & & \mu_2 + m_2 & & & & \Delta_{\text{ivc}}^- & \\ & & & \mu_2 - m_2 & -\Delta_{\text{ivc}}^- & & & \\ & & & -(\Delta_{\text{ivc}}^-)^* & \mu_3 + m_3 & & & \\ & & & & & \mu_3 - m_3 & & \\ & & & & & & \mu_4 + m_4 & \\ & & & & & & & \mu_4 - m_4 \end{pmatrix} \right] \Psi_{\mathbf{k}}, \quad (\text{S15})$$

where μ_i account for flavor-symmetry breaking, m_i correspond to intra-flavor Chern gaps, and Δ_{ivc}^\pm are the relevant inter-valley coherent terms. We remind the reader that in this matrix the blocks numbered [1, 2, 3, 4] correspond to the flavor labels $[K \uparrow, K' \uparrow, K \downarrow, K' \downarrow]$, respectively, as can be understood from the explicit form of $\Psi_{\mathbf{k}}$ in Eq. (S1). Upon diagonalization of H_{MF} , Φ may be calculated and minimized as a function of the variational parameters $\{\mu_i, m_i, \Delta_{\text{ivc}}^\pm\}$.

As an example, in Fig. S1 we present the full $T = 0$ chemical potential phase diagram for a certain choice of interaction parameters. It is this normal-state phase diagram we use for the transport calculations presented in Fig. 1 in the main text. Due to the particle-hole asymmetry, the DOS in the electron side is much larger as compared to the hole side. This results in stronger flavor-symmetry breaking, larger $|\nu| = 2$ gaps, and additional integer filling gaps on the electron side.

The existence of an insulating state at $\nu = 3$, but not at $\nu = -3$ is in line with experimental results. The larger superconducting dome at fillings $\nu = -2 - \epsilon$ as compared to $\nu = 2 + \epsilon$ which is seen in experiments, can also be understood from Fig. S1. Due to the weaker effective interactions for the holes, the occupation of the two degenerate flavors responsible for the superconductivity extends through a significant portion of the phase diagram and also to higher hole filling.

We also present a full schematic phase diagram of our model at various fillings and temperatures in Fig. S2, which reflects the main features shown Fig. 1 in the main text.

S.2. HIGH TEMPERATURE FEATURES

To elucidate some of the features observed in Fig. 1 in the main text, we plot the hole-side mean-field occupation from which Fig. 1 was compiled at two different temperatures, see Fig. S3. At zero temperature, we see a very similar behavior to Fig. 2b, with the main difference being at the Fermi level resets (around $|\mu - \mu_{\text{CNP}}|/W \approx 1, 2.4$). Since in the hole side the bandwidth is significantly larger, the Fermi level does not go down all the way to the Dirac point in this plot.

At a higher temperature we observe an appreciably different behavior. First, the low compressibility states at integer fillings (which are completely incompressible at $T = 0$) are altogether absent, as one might expect when reaching high enough temperatures. Second, the cascade of symmetry breaking is distinctive from the $T = 0$ case. At low filling, all the flavors begin to fill together, until eventually they split into two spin-valley locked sector due to the inter-valley antiferromagnetism-inducing term g_2 . Then, at intermediate filling, the flavor symmetry appears to be restored. Eventually, close to full occupation of the flat bands, we find a miniature cascade of flavor symmetry breaking, similar in nature to the one discussed in Ref. [23].

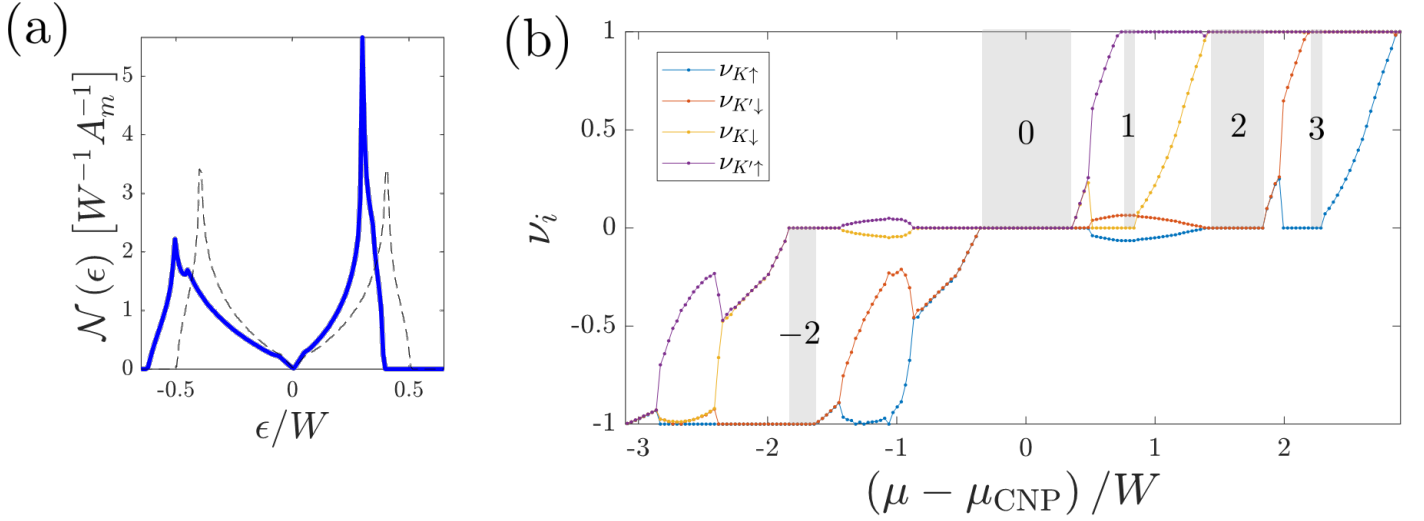


FIG. S1. (a) The DOS used for all calculations in this work (blue solid line). Notice that the hole band is significantly wider as compared to the electron one. The dashed black lines corresponds to the same DOS with $f_{p-h} = 0$, i.e., particle-hole symmetric dispersion. (b) Mean-field occupation per unit cell ν_i of individual flavors as a function of chemical potential (relative to the CNP) for $T = 0$. The same parameters as in Fig. 1 in the main text were used: $U_C = 0.72W$, $U_\delta = 0.2W$, $g_{ph,1} = g_{ph,2} = 0.12W$. Gray areas mark incompressible regions, and for each one the appropriate integer ν is denoted.

This distinctive behavior can be understood by observing that (i) the DOS is gradually increased within each flavor, and (ii) one should consider the entropy of the itinerant electron (roughly proportional to the temperature times the DOS at the Fermi level). Namely, the flavor-symmetric state at intermediate filling gains a significant amount of entropic free-energy by “de-polarizing”. This entropic contribution is eclipsed by the exchange energy at high enough filling (where the DOS is high) or at low fillings (where the DOS is too diminished to produce a sizable entropic free-energy).

The phenomenological model we present thus features phase transitions at intermediate temperatures, where the symmetries of the low and high temperature phases may be rather different. This is in fact reflected by Fig. 1 in the main text, where different patterns of low compressibility appear above $T \sim 0.05W$. For example, the Fermi level resets shown in Fig. S3b are responsible for the features apparent at the top left corner Fig. 1, as they extend slightly below $T = 0.15W$. However, we note that the specific details of this high temperature phase, e.g., where the compressibility drops are found, are much more sensitive to details of the band structure (whose features we only effectively describe), and should thus be treated with caution.

S.3. PLOTTING AS A FUNCTION OF $\tilde{\nu}$

The mean-field calculations presented in this work were all performed as a function of chemical potential μ . Instead of plotting measurable quantities as a function of μ , we wish to plot as a function of the gate-voltage V_G , which is the experimentally controlled parameter.

Although it is commonly regarded as proportional to the filling itself, ν , it is actually corrected by the quantum capacitance,

$$V_G(\nu) = \int_{\nu_0}^{\nu} d\nu' \left[C_g^{-1} + \frac{d\mu}{d\nu'} \right], \quad (\text{S16})$$

where $V_G(\nu_0) = 0$. The parameter we then plot by is

$$\tilde{\nu} = \frac{8}{V_G(\nu=4) - V_G(\nu=-4)} V_G - 4 \frac{V_G(\nu=4) + V_G(\nu=-4)}{V_G(\nu=4) - V_G(\nu=-4)}, \quad (\text{S17})$$

closely mimicking the experimental scenario. In Fig. S4 we show an example of how μ , ν , and $\tilde{\nu}$ relate to one another. Notice that ν and $\tilde{\nu}$ have a near one-to-one correspondence in metallic regions, yet this gets significantly distorted in incompressible regions, as one might surmise from Eq. (S16).

We note that in realistic experiments, effects of disorder may lead to inhomogenous broadening of certain features, e.g., insulating signatures, and further alter the measurements.

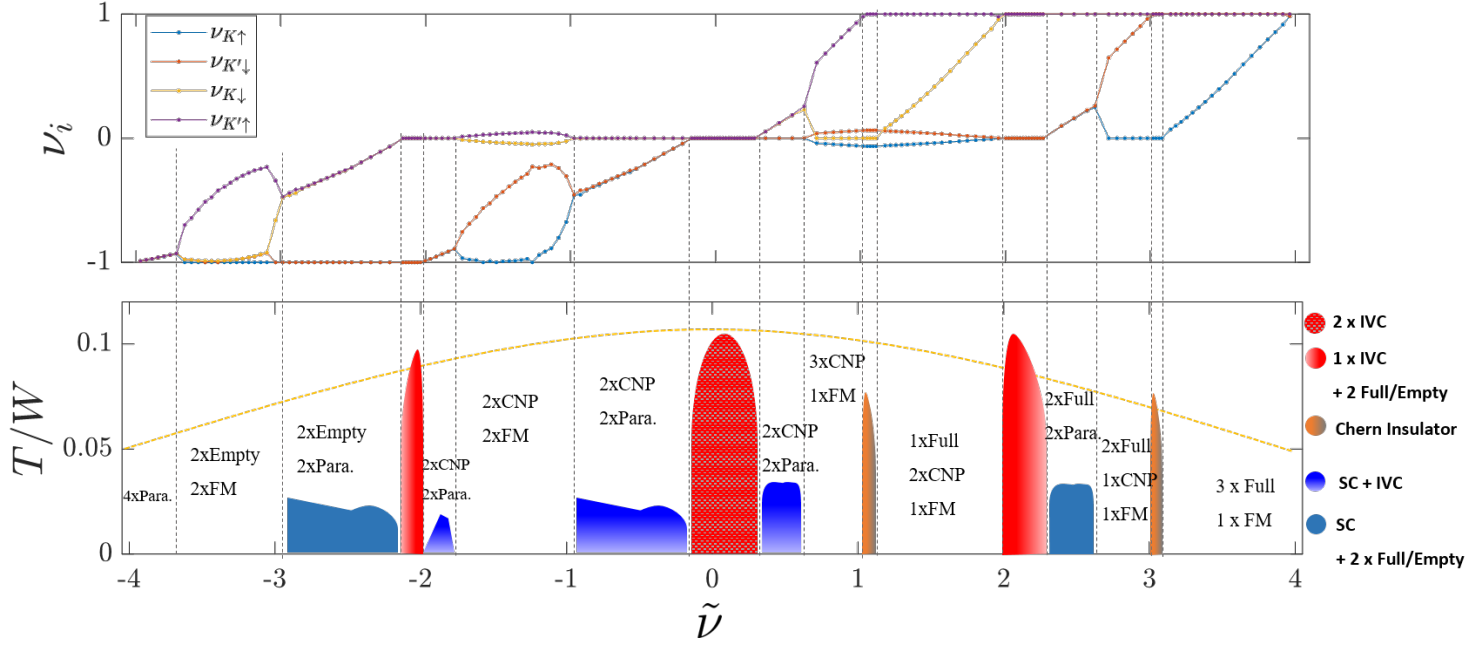


FIG. S2. Schematic phase diagram of the model presented. In the upper panel we plot the same mean-field occupation per unit cell data as in Fig. S1, as a function of $\tilde{\nu}$. The colored shape in the lower panel represent areas of incompressibility or superconductivity, with the legend appearing to the right. In the legend: IVC signals an inter-valley coherent sector, “Full/Empty” means a flavor is completely filled/empty, and “SC” stand for superconductivity. The vertical dashed gray lines in the figure mark the cascade of flavor symmetry breaking phase transitions, where each phase is labeled accordingly. Here “CNP” means a flavor is half-filled (or near the charge-neutrality point), “Para.” stands for paramagnetic (i.e., non-polarized states), and “FM” stands for a ferromagnetic phase. The dotted yellow line going over the entire phase diagram marks an approximate crossover temperature, above which the cascade of symmetry breaking transitions is qualitatively different.

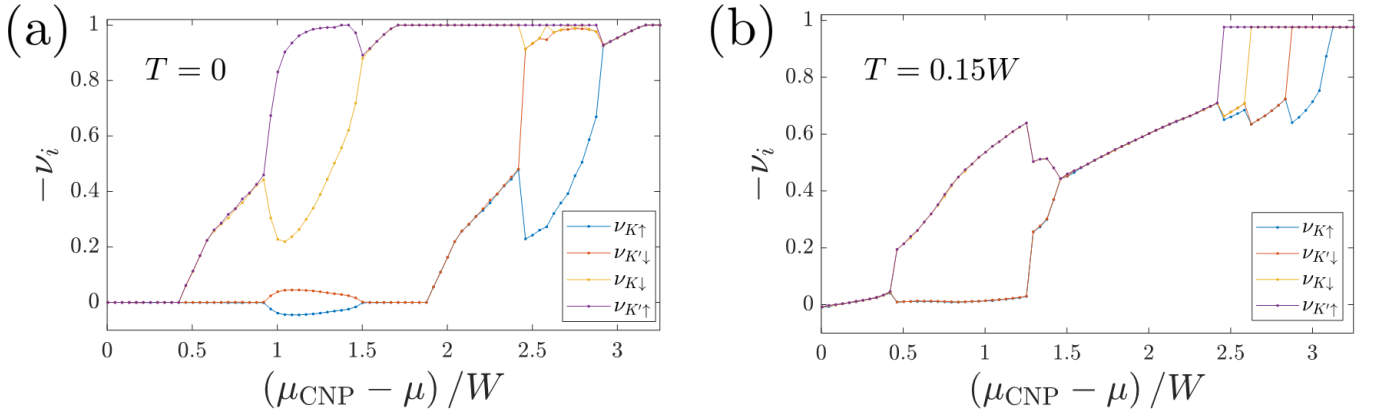


FIG. S3. Mean-field occupation per unit cell n_i of individual flavors in our model as a function of the chemical potential (relative to the CNP) on the hole-side. Notice the minus sign in both axes, indicating the doping of holes going from left to right. We have used the same parameters of Fig. 1 in the main text: $U_C = 0.7W$, $U_\delta = 0.15W$, $g_1 = g_2 = 0.12W$. In panel (a) the temperature is $T = 0$, and in panel (b) we used $T = 0.15W$.

S.4. RENORMALIZATION GROUP EQUATION FOR SUPERCONDUCTIVITY

Our starting point for deriving the RG equation (6) in the main text is the partition function

$$Z = \int D\bar{\psi} D\psi e^{-S[\bar{\psi}, \psi]}, \quad (\text{S18})$$

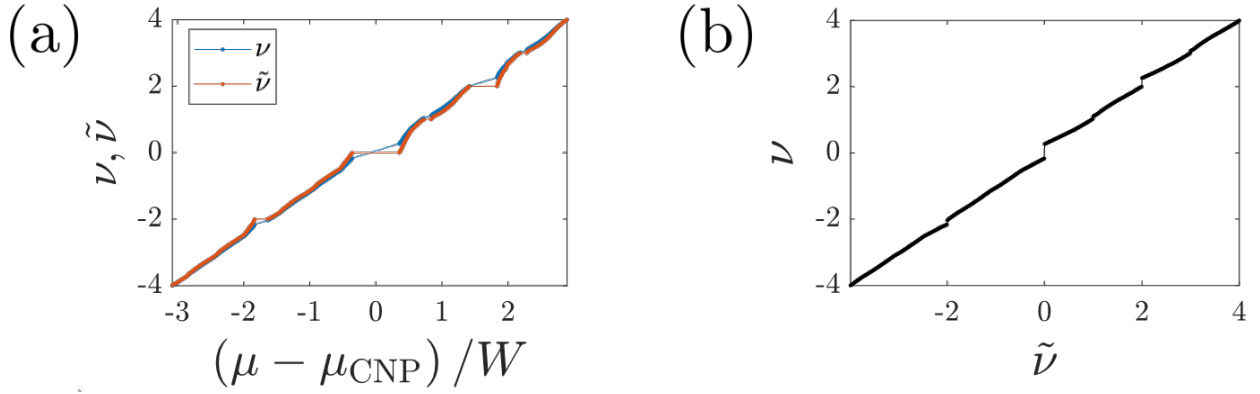


FIG. S4. (a) An example for the relation between μ , ν , and $\tilde{\nu}$ for the data presented in Fig. S1b. (b) The explicit relation between ν and $\tilde{\nu}$. The correspondence is roughly linear, and gets distorted around the less compressible (or entirely incompressible) regions.

with the action

$$\begin{aligned} \mathcal{S}[\bar{\psi}, \psi] = & \sum_{n, \mathbf{k}, \lambda} (\xi_{\mathbf{k}, \lambda} - i\omega_n) \bar{\psi}_{n\mathbf{k}\lambda} \psi_{n\mathbf{k}\lambda} \\ & + V \sum_{n, m, \mathbf{k}, \mathbf{q}} \bar{\psi}_{m\mathbf{q}1} \bar{\psi}_{\bar{m}\bar{\mathbf{q}}2} \psi_{\bar{n}\bar{\mathbf{k}}2} \psi_{n\mathbf{k}1}, \end{aligned} \quad (\text{S19})$$

where $\bar{x} = -x$, $x = m, n, \mathbf{q}, \mathbf{k}$, the field $\psi_{n\mathbf{k}\lambda}$ is a fermionic Grassman variable corresponding to a fermion with Matsubara frequency $\omega_n = (2n + 1)\pi T$, momentum \mathbf{k} , and generalized band index λ . $\xi_{\mathbf{k}, \lambda}$ are the mean-field spectra obtained from the variational calculation within our phenomenological model, and the summation over \mathbf{k} has a cut-off in energy, such that $|\xi_{\mathbf{k}}| < \Lambda$. In Eq. (S19) we assume that the interaction in the Cooper channel acts between the two relevant bands with indices $\lambda = 1, 2$, e.g., "1" = K, \uparrow , and "2" = K', \downarrow . We have also kept only the relevant zero-momentum, zero frequency component of the interaction, corresponding to a uniform superconducting order parameter.

We perform a Hubbard-Stratonovich transformation to obtain

$$Z = \int D\bar{\Delta} D\Delta D\bar{\psi} D\psi e^{-\tilde{\mathcal{S}}[\bar{\Delta}, \Delta, \bar{\psi}, \psi]}, \quad (\text{S20})$$

$$\begin{aligned} \tilde{\mathcal{S}}[\bar{\Delta}, \Delta, \bar{\psi}, \psi] = & \sum_{n, \mathbf{k}, \lambda} (\xi_{\mathbf{k}, \lambda} - i\omega_n) \bar{\psi}_{n\mathbf{k}\lambda} \psi_{n\mathbf{k}\lambda} + \frac{1}{V} \bar{\Delta} \Delta \\ & + i\sqrt{\frac{T}{\Omega}} \sum_{n, \mathbf{k}} (\bar{\Delta} \psi_{-n, -\mathbf{k}, 2} \psi_{n\mathbf{k}1} + \Delta \bar{\psi}_{n\mathbf{k}1} \bar{\psi}_{-n, -\mathbf{k}, 2}). \end{aligned} \quad (\text{S21})$$

Integrating over the fermions with $\Lambda - d\Lambda < |\xi_{\mathbf{k}}| < \Lambda$, we compare the coefficients of the $\bar{\Delta}\Delta$ term in $\tilde{\mathcal{S}}$, to find

$$\frac{1}{V(\Lambda - d\Lambda)} = \frac{1}{V(\Lambda)} + \frac{T}{\Omega} \sum_{n, \mathbf{k}}^{\Lambda - d\Lambda < |\xi_{\mathbf{k}}| < \Lambda} \frac{1}{\omega_n^2 + \xi_{\mathbf{k}}^2}. \quad (\text{S22})$$

where we have assumed $\xi_{\mathbf{k}, 1} = \xi_{\mathbf{k}, 2} \equiv \xi_{\mathbf{k}}$. Assuming the temperature is much smaller than the cutoff, we may replace the Matsubara sum with an integral to approximate the change in $V(\Lambda)$ due to the electronic contribution,

$$(dV)_{\text{el}} \approx \mathcal{N}(\Lambda) \frac{d\Lambda}{\Lambda} V^2, \quad (\text{S23})$$

with $\mathcal{N}(\Lambda)$ the electronic density of states at a distance Λ away from the Fermi energy.

We have left out of the action in Eq. (S19) the phonon-mediated interaction, $V_{\text{ph}}(\mathbf{q}, \omega) \propto \frac{1}{\omega^2 - \omega_{\text{ph}}^2(\mathbf{q})}$, where $\omega_{\text{ph}}(\mathbf{q})$ is the dispersion of the phonon branch mediating the interaction. We consider the phonons discussed in Ref. [18], with an acoustic branch which is folded into the mBZ. As a result of this folding, many "pseudo-optical" phonon branches are generated, which extend even beyond the flat-band bandwidth W . In our analysis, we do not distinguish between these different branches.

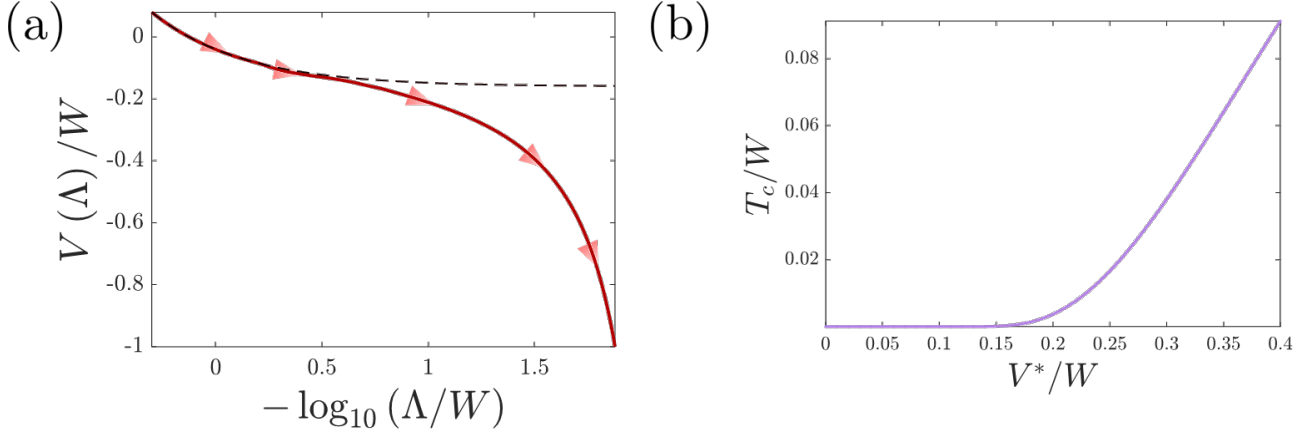


FIG. S5. (a) The RG flow of the Cooper channel interaction $V(\Lambda)$ (solid red line). The flow without the contribution of electronic screening, equivalent to taking $\mathcal{N}(\Lambda)(\Lambda) \rightarrow 0$ in Eq. (S25), is given by the dashed black line for comparison. The calculation was performed using the same parameters as in Fig. 1 in the main text, at the approximate filling $\tilde{\nu} \approx -2.4$. (b) Dependence of T_c on the strength of the phonon-mediated attraction V^* , showing a roughly linear behavior in our regime of interest, indicating strong-coupling superconductivity [57]. The same parameters as in (a) were used, with V^* varied.

Importantly, the phonon mediated interaction is attractive for $\omega < \omega_{\text{ph}}$. As we lower the energy cutoff of our fermionic model, more phonon modes satisfy this condition and contribute to the attraction. This leads to V becoming increasingly attractive,

$$(dV)_{\text{ph}} = \frac{V^*}{W} d\Lambda, \quad (\text{S24})$$

where we have implicitly assumed a constant density of states for the phonons, and $(-V^*)$ is the total contribution to the attraction strength of all the phonons with $0 < \omega_{\text{ph}} < W = \Lambda_0$. We combine the electronic and phononic contributions, Eqs. (S23), and (S24), to write the flow equation in the form presented in the main text,

$$\frac{d}{d\Lambda} V = \frac{\mathcal{N}(\Lambda)}{\Lambda} V^2 + \frac{V^*}{W}. \quad (\text{S25})$$

We note here, as we did in the main text, that Eq. (S25) suggests a critical W exists for given V_0 and V^* , below which superconductivity is absent from our calculations. Consider as an extreme example the $W \rightarrow 0$ case, where we find that if $V_0 - V^* > 0$, there can be no superconductivity, since the coupling constant remains repulsive. Too small W thus hinders the retardation mechanism in an intricate way. Yet, one should keep in mind that a reduction of W should be accompanied also by a modification of V^* and V_0 , as the phonons above the “new” reduced W should be accounted for.

This equation is to be contrasted with that of the frequently used approximation

$$\frac{dV}{d\Lambda} = \frac{\mathcal{N}(\Lambda)}{\Lambda} V^2 + \delta(\Lambda - \omega_D) V_D, \quad (\text{S26})$$

where the attractive retarded interaction V_D becomes effective “all at once” once the cutoff becomes smaller than the Debye frequency ω_D .

In Fig. S5a we plot the RG flow of $V(\Lambda)$ at a representative filling. The flow has two distinct regimes. At the higher cutoff scale, the flow from repulsive to attractive interactions is mostly due to the phonons gradually contributing. As Λ decreases, the electronic contribution takes over, leading to a divergent coupling constant. This flow highly resembles the well-known Tolmachev-Morel-Anderson paradigm of superconductivity [25, 26]. The dependence of the superconducting T_c on the phonon-induced interaction strength is demonstrated in Fig. S5b, showing a transition from exponentially small T_c , consistent with weak-coupling BCS theory, to an approximate linear dependence on V^* , indicative of a strong-coupling behavior, as discussed in Ref. [57]. We stress that this dependence is a consequence of the effective coupling constant, i.e., the DOS at the Fermi level times the attraction strength, being of order unity.

Finally, we address the issue of non-degenerate bands, i.e., $\xi_{\mathbf{k},1} = \xi_{\mathbf{k}} + \delta$, and $\xi_{\mathbf{k},2} = \xi_{\mathbf{k}} - \delta$. If the band splitting is sufficiently small, superconductivity can still be sustained. This happens near some of the superconducting domes in our calculations. For example, the left boundary of the dome near filling $\tilde{\nu} = -2 - \epsilon$ reflects the flavor-polarization shown near $(\mu - \mu_{\text{CNP}})/W \approx -2.5$. In such cases, we calculate T_c in the method we have presented for $\delta = 0$, and extract the appropriate transition temperature using the implicit relation [63]

$$\log \frac{T_c(\delta)}{T_c(\delta=0)} = \psi\left(\frac{1}{2}\right) - \psi\left(\frac{1}{2} + \frac{\delta}{2\pi T_c(\delta)}\right), \quad (\text{S27})$$

where $\psi(x)$ is the digamma function. In this formula, δ plays the role of a “pair breaking field” undermining superconductivity.

A. Analytic solution of the RG equation

The RG equation we have derived may be analytically solved in three different cases: (i) When the density of states for the electrons is constant, $\mathcal{N} = \text{const.}$, (ii) when the electronic density of state is linear in Λ , and (iii) when the phonon density of states [which is taken constant in Eq. (S25)] goes like Λ^{-1} .

For the sake of discussion, we focus on case (ii), and assume

$$\mathcal{N}(\Lambda) = \frac{p\Lambda}{W^2}. \quad (\text{S28})$$

This case is of particular importance in the system we study, as the density of states is indeed linear in certain regimes, particularly when the Fermi energy is near the Dirac points. Thus, analytic solutions of Eq. (S25) may have some qualitative relevance for the study of the MATBG phase diagram.

We find the solution of the differential equation has the form

$$W - \Lambda = W \sqrt{\frac{W}{pV^*}} \left[\tan^{-1} \left(\sqrt{\frac{p}{WV^*}} V(W) \right) - \tan^{-1} \left(\sqrt{\frac{p}{WV^*}} V(\Lambda) \right) \right], \quad (\text{S29})$$

from which we can extract the critical temperature by simplifying and setting $V(\Lambda = T_c) \rightarrow -\infty$, which produces the expression

$$T_c/W = 1 - \sqrt{\frac{W}{pV^*}} \left[\tan^{-1} \left(\sqrt{\frac{p}{WV^*}} V(W) \right) + \frac{\pi}{2} \right]. \quad (\text{S30})$$

Eq. (S30) provides us some important insights. First, we can see some trends we expected for T_c . As V^* increases, so does T_c . This is not surprising, since more phonon-mediated attraction should naturally lead to more robust superconductivity. Larger p also boosts T_c , as the electronic contribution, which is related to the density of states, is enhanced. Conversely, a larger initial repulsion $V(W)$ suppresses T_c .

More importantly, the right hand side of Eq. (S30) may become negative, indicating the absence of a superconducting instability. More concretely, this points to the existence of a critical phonon-mediated attraction V_c^* , below which superconductivity vanishes. Taking the bare repulsion $V(W) \rightarrow 0$, we can get an estimate on this critical interaction strength,

$$V_c^*/W \approx \frac{\pi^2}{4p}. \quad (\text{S31})$$

The sizable critical interaction, which is of the order of W , is due to the vanishing density of states at $\Lambda \rightarrow 0$. We point out that this result is reminiscent of Ref. [58], where it was found that the critical dimensionless coupling constant for BCS superconductivity [akin to solving Eq. (S26)] in graphene at the charge neutrality point is unity. This consequence is consistent with our treatment of the presented phenomenological model, which features no superconductivity near a Dirac point. The superconductivity in this work in the vicinity of integer fillings owes its existence to the symmetry-broken state, where electrons have a finite DOS at the Fermi level.

S.5. SUPERCONDUCTING PHASE FLUCTUATIONS

We follow Ref. [41] to elucidate the role of phase fluctuations, which lead to the Berezinskii-Kosterlitz-Thouless (BKT) phase transition, on transport. The critical temperature we derive from the RG flow equation will be labeled here as T_c , coinciding with the “bare” Ginzburg-Landau transition temperature, i.e., the critical temperature once phase fluctuations are neglected.

On the other hand, we have the BKT transition temperature T_{BKT} , which is related to T_c by

$$T_{\text{BKT}} = \frac{T_c}{1 + \tau_c}, \quad (\text{S32})$$

where τ_c is a dimensionless parameter ordinarily much smaller than unity, parameterizing the role of phase fluctuations of the superconducting order parameter. Its value may be evaluated from microscopic parameters in the clean- and dirty-superconductor

limits (where in the clean limit the mean-free-path ℓ is much larger than the Ginzburg-Landau correlation length evaluated at T_c , ξ_c , and vice-versa) [41, 59],

$$\tau_c = \begin{cases} T_c/T_F & \text{clean} \\ 0.14/k_F\ell & \text{"dirty"} \end{cases}, \quad (\text{S33})$$

with T_F the Fermi temperature, and k_F the Fermi momentum.

Examination of the experimental normal-state resistance [3, 4], as well as the superconducting correlation length [3], leads to the estimate $\ell \sim 5\xi_c$, i.e., the experimental situation appears to be closer to the clean limit. Hence, the quantity T_c/T_F will essentially determine the role and importance of phase fluctuations in transport.

The fluctuation correlation length, denoted by ξ^* , may be evaluated from the following formula for $T > T_{\text{BKT}}$ [41],

$$\xi^* = b^{-1/2} \xi_c \sinh \sqrt{b \frac{T_c - T_{\text{BKT}}}{T - T_{\text{BKT}}}}, \quad (\text{S34})$$

where b is a dimensionless constant of order unity. Notice Eq. (S34) is also valid below T_c . In fact, it is apparent that the phase-fluctuation dominant regime is the one where $T_{\text{BKT}} < T \lesssim T_c$. In other words, the parameter τ_c determines the width of a temperature “window” where fluctuations become important.

The contribution of superconducting fluctuations to the conductivity above T_{BKT} may be evaluated as [60]

$$\delta\sigma_s = \frac{e^2}{h} \frac{\pi}{8\tau_c} \left(\frac{\xi^*}{\xi_c} \right)^2. \quad (\text{S35})$$

We note that in the dirty-superconductor limit, one may write this correction in the form $\delta\sigma_s \approx 0.37\sigma_n (\xi^*/\xi_c)^2$, with σ_n the normal-state conductivity. We then arrive at an expression for the resistance,

$$R = \sigma_{\text{tot}}^{-1} = \frac{h}{e^2} \left[hD \frac{\partial n_{\text{tot}}}{\partial \mu} + \frac{\pi}{8\tau_c} \left(\frac{\xi^*}{\xi_c} \right)^2 \right]^{-1}, \quad (\text{S36})$$

with D the diffusion constant controlling the normal state resistivity. In plotting Fig. 1 in the main text we used $hD = 1 \times A_m \times W$.

Finally, let us evaluate T_F within our mean-field normal-state solution. For simplicity, let us assume a (possibly gapped) Dirac-like dispersion, such that

$$E_{\mathbf{k}} = \pm W \sqrt{\left(\frac{|\mathbf{k}|}{Q} \right)^2 + \left(\frac{\Delta_{\text{ivc}}}{W} \right)^2} - \mu_{\text{MF}}, \quad (\text{S37})$$

where W is the bandwidth, $Q \sim A_m^{-1/2}$ is the momentum cutoff, Δ_{ivc} is the normal-state IVC gap, and μ_{MF} is the mean-field chemical potential. Defining the effective mass $m^* = k_F/v_F$, with $v_F = |\partial_{\mathbf{k}} E_{\mathbf{k}}|_{|\mathbf{k}|=k_F}$, we find the Fermi temperature $T_F = (\pi \hbar^2 n^*) / (m^* k_B)$ (with n^* the carrier density),

$$T_F = |\mu_{\text{MF}}| \left[1 - \left(\frac{\Delta_{\text{ivc}}}{\mu_{\text{MF}}} \right)^2 \right]. \quad (\text{S38})$$

S.6. SUPPRESSION OF SUPERCONDUCTIVITY BY H-BN ALIGNMENT

Let us consider a scenario in which explicit sublattice-symmetry breaking is introduced via changing the single-particle part of the Hamiltonian,

$$h_0(\mathbf{k}) \rightarrow h_{AB}(\mathbf{k}) = h_0(\mathbf{k}) + \Delta_{AB} \sigma_z, \quad (\text{S39})$$

due to alignment with one of the encapsulating h-BN substrates. h_{AB} is diagonalized by the transformation

$$h_D = \mathcal{U}^\dagger h_{AB} \mathcal{U}, \quad (\text{S40})$$

with h_D a diagonal matrix, and

$$\mathcal{U} = \begin{pmatrix} \cos \theta & -\sin \theta e^{i\phi\tau_z} \\ \sin \theta e^{-i\phi\tau_z} & \cos \theta \end{pmatrix},$$

where \mathcal{U} is written in the sublattice basis, and

$$\cos 2\theta = \frac{\Delta_{AB}}{\sqrt{|\epsilon_{\mathbf{k}}|^2 + \Delta_{AB}^2}}, \quad \sin 2\theta = \frac{|\epsilon_{\mathbf{k}}|}{\sqrt{|\epsilon_{\mathbf{k}}|^2 + \Delta_{AB}^2}}, \quad \tan \phi = \frac{f_y(\mathbf{k})}{f_x(\mathbf{k})}.$$

It is now convenient to work in the conduction/valence band basis instead of the sublattice-polarized basis, i.e., working with $\Phi = \mathcal{U}^\dagger \Psi$, and projecting interactions onto one of the bands, e.g., conduction band. For the purpose of illustration, it is sufficient to consider the Cooper channel interaction term

$$\begin{aligned} U_{\sigma_x} &\equiv u \sum_{\mathbf{k}, \mathbf{q}} \Psi^\dagger(\mathbf{k}) \sigma_x \Psi(\mathbf{q}) \Psi^\dagger(-\mathbf{k}) \sigma_x \Psi(-\mathbf{q}) \\ &= u \sum_{\mathbf{k}, \mathbf{q}} \Phi^\dagger(\mathbf{k}) \mathcal{U}_{\mathbf{k}}^\dagger \sigma_x \mathcal{U}_{\mathbf{q}} \Phi(\mathbf{q}) \Phi^\dagger(-\mathbf{k}) \mathcal{U}_{-\mathbf{k}}^\dagger \sigma_x \mathcal{U}_{-\mathbf{q}} \Phi(-\mathbf{q}), \end{aligned}$$

where upon projecting to the conduction band (with fermionic annihilation operators ϕ_c), we find the interaction

$$\sum_{\mathbf{k}, \mathbf{q}} \tilde{u} \phi_c^\dagger(\mathbf{k}) \phi_c(\mathbf{q}) \phi_c^\dagger(-\mathbf{k}) \phi_c(-\mathbf{q}), \quad (\text{S41})$$

and

$$\tilde{u} = u (1 - \cos 2\theta_{\mathbf{k}} \cos 2\theta_{\mathbf{q}}). \quad (\text{S42})$$

For simplicity, we limit our discussion to the close vicinity of the Fermi surface, approximating $\epsilon_{\mathbf{k}} \approx \epsilon_{\mathbf{q}} \approx \sqrt{E_F^2 - \Delta_{AB}^2}$, leading to the approximate attenuation of sublattice-scattering interactions by

$$\tilde{u}/u = 1 - \left(\frac{\Delta_{AB}}{E_F} \right)^2. \quad (\text{S43})$$

Let us briefly summarize our findings. In the Cooper channel, the U_δ and $g_{\text{ph},1}$ interactions scatter a pair with a certain sublattice label to an opposite sublattice pair, thanks to the presence of $\sigma_{x,y}$ in the interaction. This enhances superconductivity. Alignment of the h-BN substrate introduces a σ_z term to the Hamiltonian, thereby suppressing these pairing-friendly scattering events, as the $A-B$ balance is broken. Thus, the initial electron-electron repulsion is effectively stronger, and superconductivity is suppressed.

In Fig. S6 we show the impact of the attenuation factor in Eq. (S43) on the superconducting T_c . We start with an initial repulsive interaction in the Cooper channel,

$$\tilde{V}_0 = \frac{U_C}{2} - \tilde{u}/u (U_\delta + |g_{\text{ph},1}|), \quad (\text{S44})$$

and monitor T_c at a certain filling. We note that in order to maintain the same filling with different Δ_{AB} we modify also the Fermi level. As we show in Fig. S6, there is a gradual decrease in the critical temperature with increasing Δ_{AB} , until it vanishes at some critical value of the sublattice symmetry breaking potential. The absence of superconductivity in experiments done on MATBG aligned with h-BN may then be explained by this mechanism, as the gap opened by h-BN alignment may reach an order of 15-30 meV [61], which is comparable with the bandwidth of the MATBG flat bands.

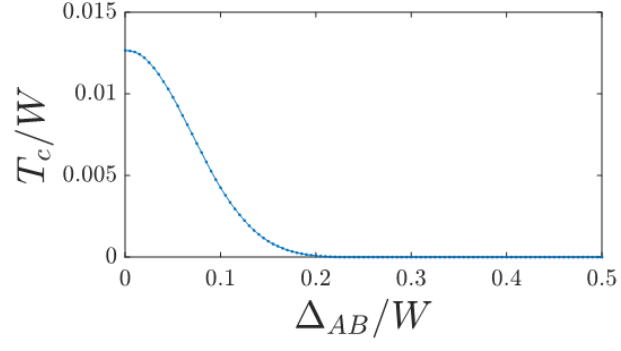


FIG. S6. Superconducting T_c as a function of Δ_{AB} , calculated at a constant filling of $n_{\text{tot}} = 2.4$, i.e., two completely filled flavors, and two degenerate opposite-valley flavors, each $1/5$ filled. Parameters used : $U_C = 0.6W$, $U_\delta = |g_{\text{ph},1}| = 0.1W$, and $V^* = 0.25W$.